Prediction of atomic H adsorption energies in metalloid doped MSSe (M = Mo/W) Janus layers: A combined DFT and machine learning study

G. Tejaswini¹, Anjana E Sudheer¹, Amrendra Kumar^{2,3}, M. Vallinayagam^{4,5}, Pavan Kumar Perepu⁶, Attila Cangi^{7,8}, Mani Lokamani⁸, M. Posselt⁸, M. Zschornak^{4,5}, C. Kamal^{2,3}, D. Amaranatha Reddy¹, and D. Murali^{1*}

¹Indian Institute of Information Technology Design and Manufacturing, Kurnool, India

⁴IEP,TU Bergakademie Freiberg, 09599 Freiberg, Germany

⁵Fakultät Maschinenbau/Energietechnik/Physik, Hochschule für Technik

und Wirtschaft, Friedrich-List-Platz 1, 01069 Dresden, Germany

²Theory and Simulations Laboratory, Theoretical and Computational Physics Section,

Raja Ramanna Centre for Advanced Technology, Indore 452013, India

³Homi Bhabha National Institute, Training School Complex, Mumbai 400094, India

⁶Indian Institute of Information Technology, Sri City, Andhra Pradesh, India

⁷Center for Advanced Systems Understanding (CASUS), D-02826 Görlitz, Germany and

⁸Helmholtz-Zentrum Dresden-Rossendorf, D-01328 Dresden, Germany

(Dated: November 21, 2025)

Janus derivatives of 2H MX₂ (M = Mo/W; X = S/Se), namely MSSe, have already been experimentally realized and explored for applications in photocatalysis, photovoltaics, and optoelectronics. Focusing on the photocatalytic properties of these layers, we investigate the adsorption of atomic hydrogen on the MSSe layers in the presence of metalloid dopants B, Si, and Ge. The layers in their pristine form exhibit positive adsorption energies (E_{ad}) , indicating an endothermic nature. Substitution of a dopant in the pristine MSSe layers alters the local symmetry, bonding character, and charge distribution, thereby increasing the number of active sites for hosting H adsorption and reducing the adsorption energy. The doping concentration and the hydrogen coverage are taken into account by considering supercells of different sizes. We select distinct sites, both atomic and interstitial, for the substitution of dopants. The spin-polarized electronic structure calculations in doped MSSe reveal a significant magnetic moment in addition to the metallic and half-metallic nature. The energetics of the H atom at various sites is studied to find the most favorable active site on the MSSe Janus layers. Our results based on density functional theory (DFT) calculations show that the adsorption process becomes spontaneous and less attractive in the presence of atomic site dopant substitution, whereas the interstitial site results in an endothermic behavior. Moreover, having the data from DFT, we develop a supervised machine learning (ML) model for predicting the hydrogen adsorption energy, E_{ad} . We propose an ML model based solely on elemental features for predicting E_{ad} in doped monolayers. For this purpose, we utilize 23 elemental features of the atoms involved in the structure, thereby eliminating the need for DFT calculations in feature design. The dimensionality reduction technique, principal component analysis (PCA), is employed to reduce the dimensionality of the feature space, yielding independent features that are mutually orthogonal. The model is implemented as a multi-layer perceptron regressor with two hidden layers. The data augmentation technique is employed to artificially expand the dataset size, thereby enhancing the accuracy of the neural network model by 0.90% on the testing data.

I. INTRODUCTION

In the post-graphene era, transition metal dichalcogenides (TMDs), characterized by the MX₂ (M- transition metal, X - chalcogen) stoichiometry and semiconducting property [1, 2] have emerged as a new class of prospective 2D materials, since the exfoliation of graphene layers from graphite [3]. Unlike graphene, which does not possess a band gap, TMDs are characterized by band gaps, which can be tuned by increasing or decreasing the number of layers, making them suitable for various optoelectronic applications such as photo detectors [4], light-emitting diodes [5], solar cells [6], and water splitting driven by visible light [7]. The materials studied most extensively in the TMD class are MX₂,

where M = Mo/W; X = S/Se [8]. The most stable phase of MX₂ TMDs is the trigonal prismatic phase, with single M and six X atoms located at the center and corners of the prism. Recently, polar TMDs known as Janus layers (JLs), which are derived from traditional TMDs, have gained a lot of attention due to the asymmetry-induced enhanced properties, such as Rashba spin splitting [9, 10], second harmonic generation [11, 12], skyrmionics [13, 14], excitonic [15–17], thermoelectric [18–21] and 2D magnetic ordering [22, 23]. JLs can be formed by substituting one of the two X atomic layers in MX₂ structures with the other chalcogen atomic layer of different electrongativity. Due to the difference in the chemical environment on either side of the central metal atomic layer, the out-of-plane mirror symmetry is broken, resulting in an intrinsic dipole moment along the direction perpendicular to the layer [24]. Such out-of-plane polarization in the JLs facilitates the spatial separation of the photogenerated electron-hole pairs, thereby minimizing their

^{*} dmurali@iiitk.ac.in

recombination. Thus, JLs are well explored for photocatalytic water splitting and photovoltaic applications [25–29]. The first and widely explored layers of this kind are transition metal-based JLs with the MXY stoichiometry, where $M=Mo,\ W;\ X/Y=O,\ S,\ Se,\ Te\ [30–33].$ Given the experimental challenges in synthesizing JLs, theoretical investigations serve as a powerful approach to explore and predict their fundamental properties and potential functionalities. To date, the following three JLs MoSSe [34, 35] WSSe [36] and PtSSe [37] are synthesized.

In the current scenario, the world economy is lagging in the production of green hydrogen to achieve net zero emissions goals [38]. Photocatalytic water splitting is a method that requires only sunlight and a semiconducting photocatalyst. Understanding the adsorption energetics of the intermediates involved in photocatalytic water splitting is crucial for increasing the efficiency and yield of the photocatalyst. Herein, we focus on the adsorption of H atoms, a crucial step in the sub-reaction known as the hydrogen evolution reaction (HER) in photocatalytic water splitting. The H adsorption process can be characterized by calculating the adsorption energy (E_{ad}) , which can be defined as $E_{ad} = E_{H*}$ - E_* - 0.5 E_{H_2} [39]. Here, E_{H*} and E_* are the total energies with and without adsorbed H atom at the active site (*) of the JL, and E_{H_2} is the total energy of the H₂ molecule. The atomic H adsorption reaction is reported to be endothermic in both the regular MX₂ and Janus MXY layers [40], which limits the efficiency of solar-driven hydrogen production [41]. To improve the performance, various structural modification techniques can be adopted, such as heterostructure construction [42–45], strain modulation [46, 47], vacancy creation [48–50], and doping of a metallic or non-metallic element [51, 52]. Employing these structural modification techniques not only increases the number of active sites for adsorption but also improves the straddling band alignment and enhances the efficiency of light absorption.

In this study, we focus on the substitutional doping at various atomic and interstitial sites of the MSSe JLs. The breaking of the local surface symmetry by introducing a dopant will highly impact the electronic, optical, and adsorption properties [53, 54]. We consider the metalloid elements B, Si, and Ge as dopants, which are nontoxic. The screening of efficient photocatalysts via an experimental synthesis approach is a time-consuming and resource-intensive process. In general, DFT-based calculations can predict several physical properties of new materials and provide a microscopic understanding of observed physical properties. However, one has to work with larger supercells to reduce finite-size effects [55], which renders the simulations computationally demanding. Thus, emerging machine learning methods have become indispensable tools to speed up the screening process, e.g., by employing models tuned to predict desired properties, which are trained on large datasets [56]

In recent years, numerous machine learning (ML) techniques have been developed for predicting various atomic and molecular adsorption energies. For example, the

molecular CO₂ and CO adsorption energies in binary alloys have been studied with the physicochemical properties of the material using a neural network based on multi-layer perceptrons, decision tree regression, support vector regression, and extreme gradient boosting [57]. The atomic H adsorption energies have been studied on Pt nanoclusters with the help of local structural features and with Gaussian Process Regression, and Random Forest Regression methods [58]. By taking the electronic density of states (DOS) of the surface atoms as input, the adsorption energies of monoatomic elements H, C, N, O, S, and their hydrogenated counterparts, CH, CH₂, CH₃, NH, OH, SH on the bimetallic alloy surfaces have been predicted accurately using the convolution neural networks [59]. The adsorption of various molecules, including H₂, CH₄, CO₂, and biogas in metal organic frameworks has been studied using ML models [60]. The adsorption energy predictions of various transition metal atoms on the MX_2 , where M = Mo/W; X = S/Se transition metal dichalcogenide monolayers in the presence of X point defects, have been done using the Sure Independence Screening and Sparsifying Operator (SISSO) generated features [61]. Using the same SISSO technique, the molecular adsorption energies of various molecules, including H₂O, CH₃, CO, N, NH, NH₂, NO, O, and OH on various transition metal surfaces are studied, and the importance of the d-band center combined with the surface energy is explored for better adsorption energy predictions [62]. Adsorbate Chemical Environment-based Graph Convolution Neural Networks (ACE-GCN) have been introduced for the accurate prediction of the adsorption energies for various adsorbates on the Pt₃Sn allov and Pt facet [63]. Using 15 chemical features and the ML models Gradient Boosted Regression, Random Forest Regression, K-nearest neighbours, Adaptive Boosting, and support vector regression, the Gibbs free adsorption energy is predicted in the transition metal doped WSn₂N₄ 2D layers [64].

In the present work, extending the work of Vallinayagam et al. [65], where they studied the atomic H adsorption in the doped MoSSe layer in the $4\times4\times1$, we predict the H adsorption energy at various sites using ML techniques on the MSSe JLs, in the presence of three dopants, B, Si, and Ge, substituted at distinct sites. We consider two different doping concentrations 2.1% and 3.8%, and study the effect on H adsorption. To date, there are no reports available that predict the H adsorption energies using ML in the doped MSSe JLs, including the dependence on the doping concentration. As descriptors for the ML model, we utilize the chemical features of the elements, which require no computational effort. The present work is structured as follows. Initially, we discuss our DFT results, which include the binding energy, charge transfer, spin polarization, density of states, and the H atom adsorption energies in doped MSSe layers. Followed by this, discuss the feature selection and the physical importance of features in predicting the H adsorption energy. We discuss our dimensionality reduction

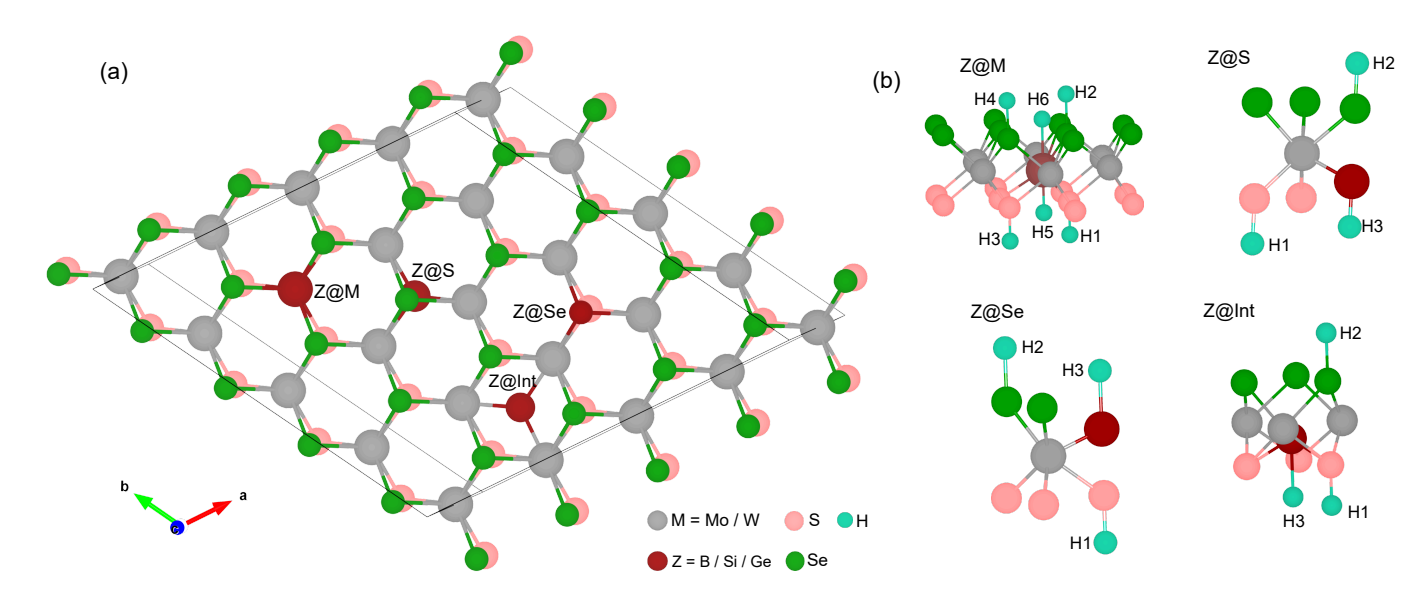


FIG. 1. Schematic illustration of (a) Z doping at various atomic sites in the MSSe JL and (b) H adsorption sites in Z-doped MSSe JLs. By convention, H1 and H2 denote H atoms adsorbed atop S and Se sites, respectively. H3 and H4 represent adsorption at the top of the dopant Z, with H approaching through the S and Se planes, respectively. For the Z@Mo configuration, two additional adsorption sites, located on the S and Se planes away from the dopant, are also considered. The same set of adsorption sites is used for both the $3 \times 3 \times 1$ and $4 \times 4 \times 1$ supercells.

technique, based on principal component analysis (PCA), to reduce the dimensionality of the original feature space. We present the implementation of the neural network model and its prediction performance. Finally, we discuss expanding the dataset using the synthetic minority over-sampling technique for regression (SMOTER), and the performance of the neural network model on the combined dataset of original and synthetic data points has been tested.

II. COMPUTATIONAL METHODS

Spin-polarized electronic structure calculations based on DFT have been carried out using the Vienna ab-initio simulation package [66]. The electron-ion interaction is treated within the projector-augmented wave (PAW) method [67], where plane-waves are generated with the cutoff energy of 600 eV. For exchange-correlation functional, we employ the Perdew-Burke-Ernzerhof (PBE) functional within the generalized gradient approximation (GGA) [68] scheme. As a common condition, the forces on atoms are relaxed down to the accuracy level of $1\times 10^{-3}\,\mathrm{eV}\,\text{Å}^{-1}$ and the energy convergence criteria is set as $1 \times 10^{-6} \, \text{eV}$. To determine the H adsorption energy at different H concentration and doping concentration levels, supercell sizes of $3\times3\times1$ and $4\times4\times1$ were considered for the calculations with a vacuum of 15 Å in the direction normal to the layer to avoid the interactions with repeated images. The integration in the reciprocal space is carried out on $3\times3\times1$ and $5\times5\times1$ k-point grid (adapted depending on simulation cell size) generated within Monkhorst–Pack scheme [69]. The dopant is

introduced in these cells by replacing one of M/S/Se, see Fig. 1(a), by the dopant Z, thereby yielding the doping concentration of 2.1% and 3.8%. Different H adsorption sites on and near the dopant, Fig. 1(b), are considered to generate the required dataset for further ML modeling. The E_a^H is calculated for all H adsorption sites in two doping concentrations to infer the effect of doping concentration in predicting the E_a^H .

III. RESULTS AND DISCUSSION

A. Dopant binding in MSSe JLs

The stability and interaction of the dopant in MSSe JLs are analyzed by the binding energy per atom E_b of Z with the host layers. The E_b is calculated by the expression,

$$E_b = \frac{1}{N} (E_{\text{Z-MSSe}} - n_{\text{M}} \cdot E_{\text{M}} - n_{\text{S}} \cdot E_{\text{S}} - n_{\text{Se}} \cdot E_{\text{Se}} - n_{\text{Z}} \cdot E_{\text{Z}})$$
(1)

where $E_{\text{Z-MSSe}}$ is the ground state energy of Z doped MSSe layers. The ground state energies E_{M} , E_{S} , E_{Se} , and E_{Z} of bulk crystals or dimers of M, S, Se, and Z elements, respectively. The total number of atoms N taken in the simulation is equal to the sum of the number of individual atomic species n_{M} , n_{S} , n_{Se} , and n_{Z} . The bulk crystals of Mo (space group: 229; symmetry: $\bar{\text{Im}}3\text{m}$), W (space group: 229; symmetry: $\bar{\text{Im}}3\text{m}$), B (space group: 166; symmetry: $\bar{\text{R}}3\text{m}$), Si (space group: 227; symmetry: $\bar{\text{Fd}}3\text{m}$) are used to get their ground state energies. For chalcogens,

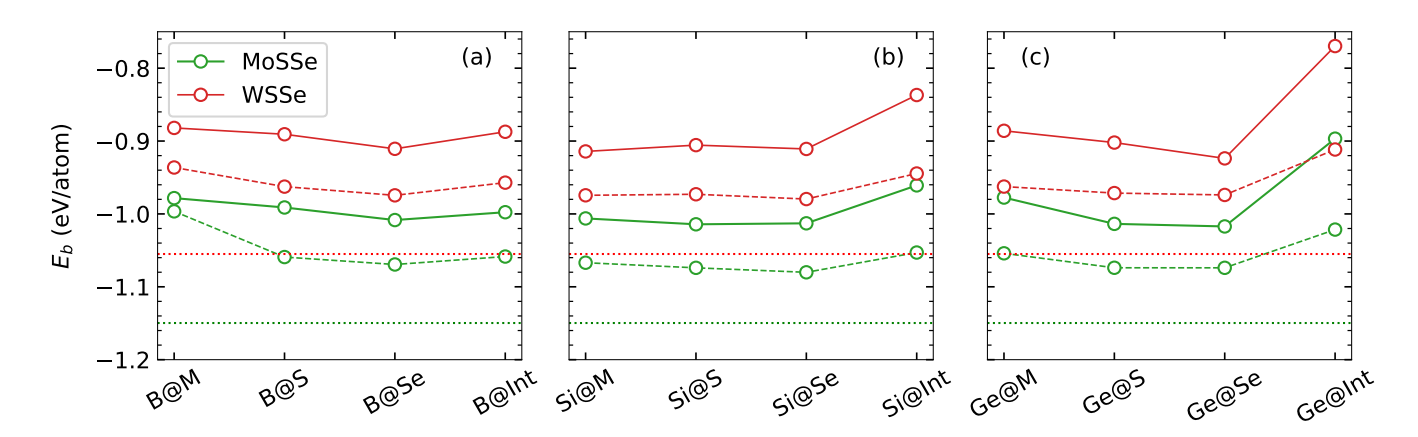


FIG. 2. Calculated binding energy E_b of (a) B, (b) Si, and (c) Ge doping in MoSSe (green lines) and WSSe (red lines) host layers. Driven by the atomic size effect, the binding strength in Z@Int doping is less than that in the remaining doping sites, except for the B dopant. Overall, the chalcogen sites are the energetically preferred doping sites. The Z@M notation denotes doping at Mo in MoSSe and W in WSSe atomic sites. The continuous and dashed lines represent the E_b calculated with $3 \times 3 \times 1$ and $4 \times 4 \times 1$ cells, respectively. The dotted red and green lines represent the binding energy of pristine MSSe layers, respectively.

 S_2 and Se_2 dimers are considered. The calculated E_b is shown in Fig. 2. According to the definition in Eq. 1, a negative (positive) E_b denotes an attractive (repulsive) interaction between the dopant and host layer, indicating a stable (unstable) doping scenario. As shown in Fig. 2, all doping scenarios yield negative E_b , exposing a stable and energetically feasible dopants and doping configurations for MSSe JLs. Particularly, the dopants are more stable at chalcogen sites. In comparison, the $4 \times 4 \times 1$ supercell yields a better E_b prediction than the $3 \times 3 \times 1$ supercell. For reference, we also plot the binding energy of pristine MSSe with the green and red dotted lines in Fig. 2. As expected, the pristine MSSe layers show larger binding energies compared to the doped layers.

The atomic size of the dopant strongly influences the E_b . For instance, B shifts toward the S atomic plane due to its small size in B@Mo doped layer. Also, B intercalates favorably at the interstitial site, turning the E_b comparable to that of B@S doping. In contrast, larger dopants such as Si and Ge are energetically less stable at interstitial positions, see Fig. 2. Furthermore, dopants induce charge redistribution, activating the nearest-neighbour atoms, while atoms beyond the first coordination shell recover their pristine charge state, as in undoped MoSSe. This behavior is particularly pronounced for Z@Mo doping [65] and is expected to occur similarly in Z-doped WSSe layers.

B. Charge density in doped MSSe

To understand charge redistribution when a dopant atom is introduced at distinct sites of the MSSe Janus layers, we calculate the differential charge density (DCD). As a representative case, we present the DCD in the MoSSe when dopants B, Si, and Ge are introduced at the

Mo, S, Se, and interstitial sites, which is shown in Fig. 3. From the valence electron number of B (3: $2s^22p^1$), Si(4: $3s^23p^2$), and Ge(4: $4s^24p^2$), we expect that the doping in MSSe leads to p-type doping. But, on the contrary, depending on the doping site, the properties of the dopants result in both p-type and n-type doping. It is clear from Fig. 3 that the charge redistribution is confined only around the dopant, and the atoms that are far from the dopant have not been affected. The presence of dopants in the MSSe layers redistributes the charges in the nearby atomic sites, tuning them as activated sites [65]. Since the HER is an electron-demanding reaction, the n-type doping in MSSe layers is favorable.

In the case of Z@Mo (Mo: 4d⁵5s¹), a similar trend of charge distribution is seen for B, Si, and Ge. The charge depletion is found near the dopant atom and is being transferred to the S and Se atomic planes. However, due to the large electronegativity of S atoms, more charge accumulation is seen towards the S atomic plane compared to that of Se. From the observed charge distribution, we can infer that doping the Z@M site of MSSe leads to n-type doping. The pronounced interaction between the dopant and the first nearest Mo and S atoms surpasses the Z-Se interaction. Specifically, the charge distribution is markedly concentrated along the Z-S bond. Conversely, the Z-Se interaction is scarcely perceptible, reinforcing the assertion that the Z-S interaction prevails over the Z-Se interaction. Consequently, the S sites emerge as more optimal for the HER compared to Se. Therefore, the electronegativity and atomic size differences between the dopant and host atoms alter the charge states of nearby chalcogens, making them a favorable site for HER activity.

When B is introduced in the $S(3s^23p^4)$ atomic plane, the electron accumulation is seen near the B atom (-0.33 e), which is confirmed by Bader analysis. Thus, dop-

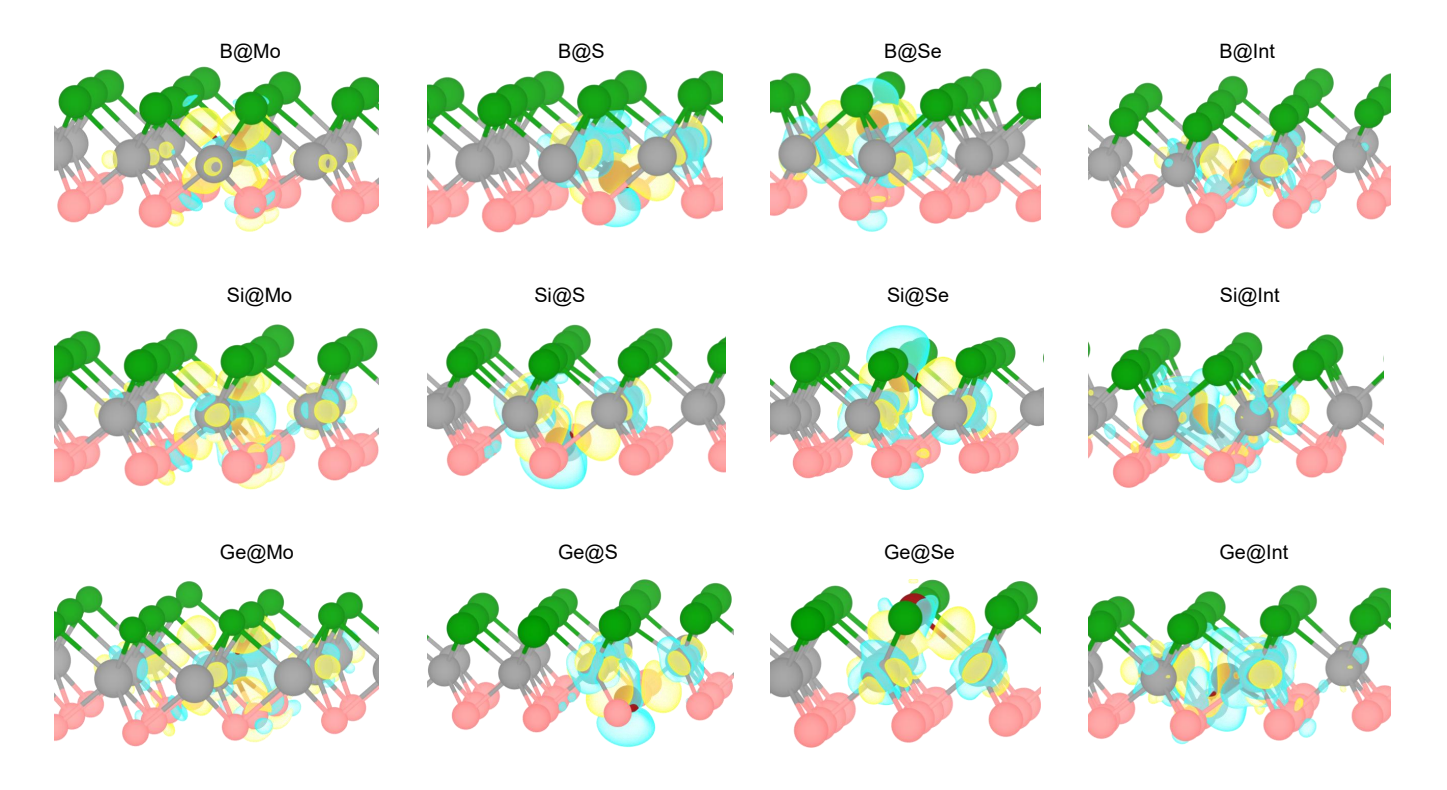


FIG. 3. Calculated differential charge density for B, Si, and Ge doped MoSSe JL, respectively. The differential charge density is defined as $\rho(Z + MoSSe) - \rho(MoSSe) - \rho(Z)$. Here $\rho(Z + MoSSe)$ and $\rho(Z)$ are the charge densities of doped MoSSe and dopant, respectively. The term $\rho(MoSSe)$ represents the charge density of dopant removed MoSSe JL.

ing B at the S site of MoSSe leads to p-type doping. In contrast to the B, the doping of Si and Ge at S shows electron depletion near the dopant and accumulation on the first nearest neighbour three Mo atoms. Therefore, the dopants Si and Ge act as donors when introduced at the S atomic plane. From Fig. 3 it is clearly evident that the introduction of the dopant in the S atomic plane does not influence the charge distribution on the Se(4s²4p⁴) atomic plane. A similar distribution of charge is observed for the doping of Z in the Se atomic plane as that of the Z doping in the S atomic plane. The dopant B, by accepting the charge, leads to p-type doping, while Si and Ge, by depleting the charge, result in n-type doping. When the doping at the interstitial site is concerned, the three dopants, B, Si, and Ge, donate charge, which is distributed across the interstitial region and has not transferred to either of the S or Se atomic planes as observed from Fig. 3. The presence of the dopant at distinct atomic and interstitial sites alters the local bonding character and charge distribution within the structure, which in turn induces spin polarization and significantly affects the electronic properties of the structure.

C. Magnetic moment and electronic structure of doped MSSe

The spin-polarized electronic structure calculations reveal the presence of defect states within the band gap for all doped systems. The observed GGA band gaps of pristine MSSe are 1.56 eV and 1.69 eV, respectively. From the electronic DOS (see Fig. 4 and SFig. 1-3), it is clear that the impurity states are present near the Fermi level, which reduces the original band gap of MSSe. With respect to the size of the chosen supercell, the DOS of doped MSSe shows dissimilar trends. However, for a particular size of the supercell, the MSSe DOS show similar behaviour. As a representative case in Fig. 4, we present the atom-resolved DOS for the Z doping in a $4\times4\times1$ supercell of MoSSe, representing the doping concentration of 2.1%. From Fig. 4, it is observed that the doping of B at all the considered four distinct sites shows a shift between the spin-up and spin-down states, resulting in a net magnetic moment. The observed magnetic moments are given in Table I. In the case of B doping, the highest magnetic moment is observed for B@Mo doping, with a value of 1.64 μ_B . The major contribution to this moment comes from the Mo-d (1.10 μ_B) orbitals with a small contribution from the S-p and Se-p orbitals $(0.24 \ \mu_B)$, as also evident from the spin density given in SFig. 6. The moments are mainly localized around

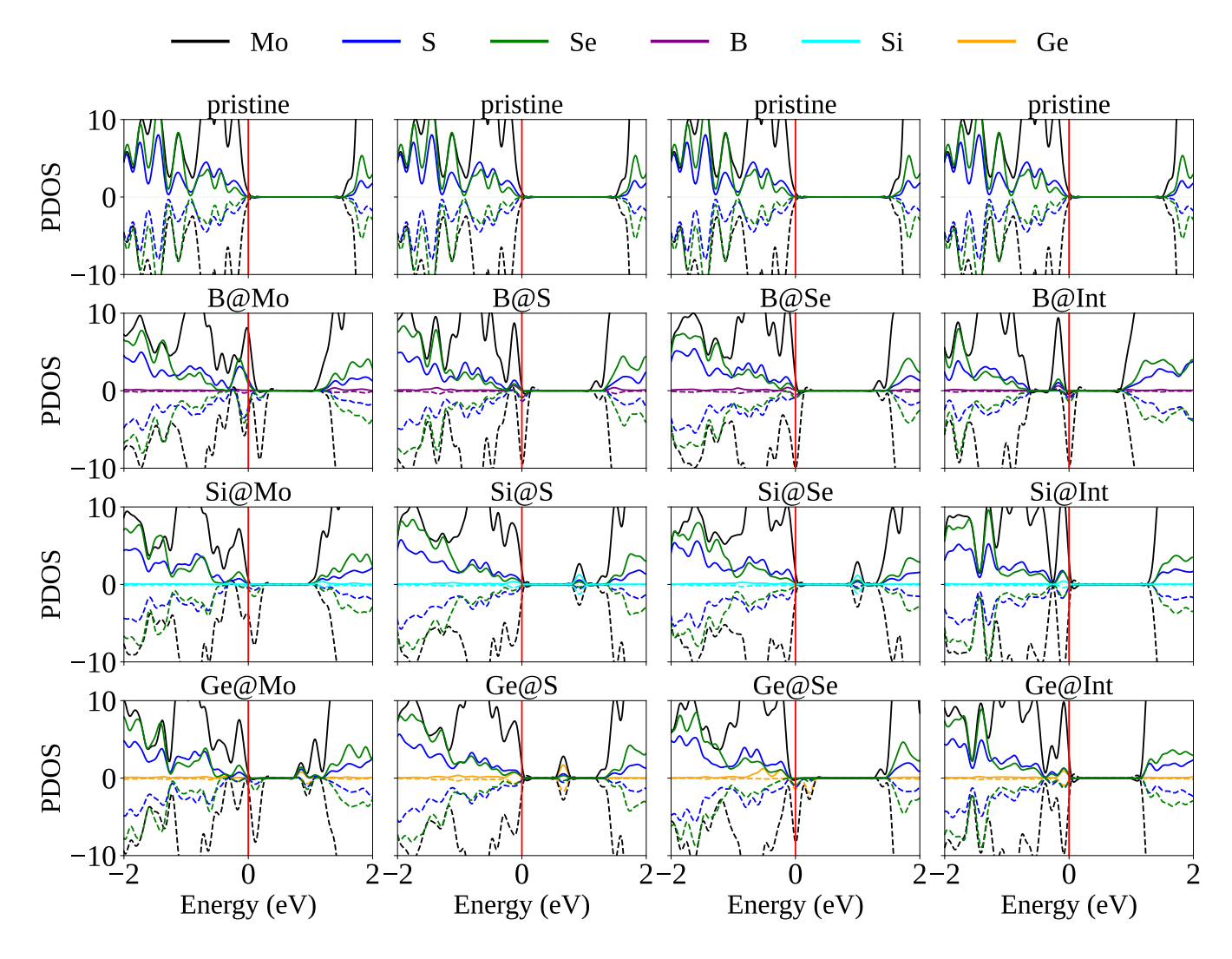


FIG. 4. Atom resolved density of states of pristine and B, Si, and Ge doped MoSSe layer at a doping concentration of 2.1% ($4\times4\times1$ supercell). The solid red line represents the Fermi-level.

six Mo atoms, which are the second-nearest neighbours to the dopant B. In the case of B@S, B@Se, and B@Int as well, the magnetic moment is mainly induced due to the Mo-d orbitals. Overall, doping B in MoSSe at four distinct sites has resulted in a metallic behavior due to the crossing of Mo-d states above the Fermi level. Spin-up carriers dominate the conducting channel in B@Mo, while the down-spin carriers provide channels for B@S, B@Se, and B@Int.

Belonging to the same group in the periodic table, having the same number of valence electrons, the doping of Si and Ge shows a similar trend in the magnetic moment and electronic structure for doping at distinct sites in MoSSe (as well as in WSSe), except for the doping in the Se atomic plane. In the case of Si(Ge) doping at the Mo site, MoSSe shows half-metallic behavior due to the Fermi crossing of the spin-down Mo-d state and has resulted in a net magnetic moment of 2.02 (2.03) μ_B . The corresponding spin density is shown in SFig. 6, which

indicates an intense spin polarization on the first nearest three Mo atoms. The doping of Si at S, Se, and interstitial sites has resulted in zero magnetization, and MoSSe exhibits semiconducting behavior with band gaps of 0.93 eV, 1.00 eV, and 1.38 eV, respectively. The doping of Ge@S and Interstitial sites shows zero magnetic moment, and the band gaps are 0.67 eV and 1.25 eV, respectively. However, in the case of Ge@Se, we observe a magnetic moment of 2.00 μ_B and half-metallic behaviour with the Fermi crossing of the Mo-d states and Ge-p states. The observed magnetic moments reflect this with net magnetization of the MoSSe having main contributions from the Mo-d $(0.90~\mu_B)$ and Ge-p $(0.54~\mu_B)$ orbitals.

A similar trend to that of the $4\times4\times1$ supercell of MoSSe in terms of magnetic moment and band gaps is observed in the $4\times4\times1$ WSSe Janus layer as well, which are provided in SFig. 3 and SFig. 7. However, the largest magnetic moment of 3.03 μ_B is found in WSSe in the case of B doping at the W atomic site, which is mainly

coming from the W-d (1.49 μ_B) and S-p and Se-p (0.56 μ_B) states. The observed spin densities and the electronic DOS for the $3\times3\times1$ supercells of MSSe are given in SFig. 1-2 and SFig. 4-5.

D. H atom adsorption energies in MSSe JLs

In the ref. [65], we have discussed the behavior of the H atom in the MoSSe JL in the presence of the metalloids B, Si, and Ge, doped at distinct atomic and interstitial sites at a doping concentration of 2.1%. In this study, a similar schematic is applied to investigate the effect of dopant concentration on H adsorption in MSSe JLs (M = Mo, W). The dopants are substituted in MSSe at four different sites, as mentioned in Fig. 1 (a). By analyzing the charge distribution in Z doped JLs, various feasible H adsorption sites are selected and the selection is depicted in Fig. 1(b). Furthermore, these simulations explore the effects of doping concentration and H coverage on the adsorption energy of H, which are internally controlled by cell size. The doping concentrations of 2.1% and 3.8% are finally achieved, and the H adsorption behavior is analyzed for each doping scenario. The interaction of atomic H with distinct sites on the MSSe Janus layers is probed by calculating the adsorption energy, which can be defined as

$$E_{ad} = E_{Z@MSSe+H} - E_{Z@MSSe} - \frac{1}{2}E_{H_2}$$
 (2)

Where $E_{Z@MSSe+H}$, $E_{Z@MSSe}$ are the total energies of the Z-doped MSSe layer energies with and without H atom adsorption, and E_{H_2} is the total energy of the H_2 molecule. The positive and negative values of E_{ad} indicate endothermic and exothermic behavior of H on the MSSe layers. For the optimal HER, we require such scenarios where the \mathbf{E}_{ad} is only slightly negative. Too large a negative E_{ad} also indicates the strong binding of H towards the surface, which is not favorable for HER, since the second step of HER, known to be the H₂ releasing step, will become challenging. In pristine MSSe, the values of E_{ad} for the H adsorption on top of the S (Se) atom are found to be 1.67 eV (2.19 eV) and 1.90 eV (2.12 eV), respectively, in a $4\times4\times1$ supercell [65, 70]. In the case of a $3\times3\times1$ supercell of pristine MSSe layers, the E_{ad} values for the adsorption on top of the S (Se) atom are 1.61 eV (1.88 eV) and 1.89 eV (2.03 eV), respectively [70]. The E_{ad} values indicate an extensive repulsive interaction of H in pristing MSSe under the H coverage of 2.08% ($4\times4\times1$ supercell) and 3.70% (3×3×1). Herein, we discuss the trends in E_{ad} with respect to the site of the dopant.

1. Doping at M site

In the Z@M scenario, the selected dopants are substituted at the M site in MSSe JLs, irrespective of differences in the atomic size of the dopant and host atoms.

The Z@M doping alters the charge distribution and coordination with nearest neighbours due to the size effect. For example, B@Mo in MoSSe JL reduces the effective coordination due to the shift of B towards the Satomic plane [65]. These changes in dopant sites after the charges on constituent atoms, producing activated sites. The six distinct sites considered for the H adsorption are shown in Fig. 1(b). The H adsorption on the dopant has two possibilities, where H can interact through either the S(5) or the Se(6) plane. The calculated E_{ad} for the six distinct H adsorption sites in the Z@M doping case are given in Fig. 5. In the MoSSe JL, at 2.1% doping concentration (DC), the adsorption energy for sites 3 and 4 is the same as that for 5 and 6 when the doping atom is B or Ge. But this is not the case with Si, where all six sites differ in E_{ad} . However, E_{ad} differs for all six sites in the WSSe JL for both DCs. For B@Mo doped MoSSe JL, the chemisorption dominates at a DC of 2.1% for all four sites with a large negative E_{ad} , which indicates the strong binding of H with the layer and is not favorable for HER. For the same B@Mo case, at 3.8% doping, the mentioned six distinct sites show different E_{ad} . For site 2, the E_{ad} is slightly negative, indicating spontaneous H adsorption and a less negative value, which favors HER. For B@W of WSSe JL, the adsorption of H is endothermic for sites 2, 3, and 4, whereas it is exothermic for sites 1, 5, and 6 at a DC of 2.1%. The sites 2, 3, and 4, which represent the H adsorption on the immediate Se neighbour and the next appearing S and Se neighbours to the dopant, possess the same charge as that in the case of pristing WSSe. This is due to the charge delivered by the B atom being mainly transferred to the first nearest. highly electronegative three S atoms, as is evident from the Bader analysis. On top of the dopant atom from either of the sides, S and Se E_{ad} values are found to be negative, which indicates that the B-H bond is stronger than that of the S-H and Se-H bonds. The H adsorption on S is favourable only when the dopant is acting as a donor in the MSSe layers. At a doping concentration of 3.8%, all sites show positive \mathbf{E}_{ad} with sites 2 and 5 having E_{ad} close to zero, and the E_{ad} for site 2 is found to be slightly negative (-0.04 eV). At 3.8% DC of B@Mo of MoSSe and B@W of WSSe, the E_{ad} shows exactly similar behavior for both MSSe for all six sites. This is not the same for the DC 2.1%.

In the case of Si@Mo in MoSSe, for the two DC levels, the E_{ad} shows a similar behavior except for the case of site 5. For site 5, i.e., on top of the Si atom facing the S-atomic plane, the E_{ad} is 1.23 eV for the 2.1% DC, and it is -0.47 eV for 3.8% DC. For the Si@W in WSSe, the H adsorption is endothermic for sites 3, 4, and 5, whereas it is exothermic for sites 1, 2, and 6. The E_{ad} for sites 3 (0.73 eV) and 4 (1.40 eV) at 2.1% DC is increased by 0.10 and 0.13 eV for the DC of 3.8%. Similarly, for sites 1 and 2, E_{ad} increased by an amount of 0.11 and 0.09 eV, respectively, from the DC 2.1% to 3.8%. At the DC of 2.1%, E_{ad} is negative, indicating the exothermic reaction for sites 2 and 6, and these reactions became endothermic

TABLE I. Magnetic moment m and	band gap E_g informatio	n for the MSSe JLs	s with the dopant s	substitution at distinct sites
and concentration levels.				

S.No	Structure	Dopant	$m (\mu_B)$	E_g (eV)	S.No	Structure	Dopant	$m (\mu_B)$	$E_g \ (eV)$
1		B@Mo	0.99	0.00	25		B@Mo	1.64	0.00
2		B@S	0.00	0.01	26		B@S	1.10	0.00
3		B@Se	0.97	0.00	27		B@Se	1.03	0.00
4		B@Int	0.92	0.00	28		B@Int	1.06	0.00
5	$3 \times 3 \times 1$	Si@Mo	1.90	0.03	29	$4 \times 4 \times 1$	Si@Mo	2.02	0.00
6	MoSSe	Si@S	0.00	0.77	30	MoSSe	Si@S	0.00	0.93
7	Mosse	Si@Se	2.07	0.00	31	Mosse	Si@Se	0.00	1.00
8		Si@Int	0.00	1.37	32		Si@Int	0.00	1.38
9		Ge@Mo	1.87	0.00	33		Ge@Mo	2.03	0.00
10		Ge@S	0.00	0.49	34		Ge@S	0.00	0.67
11		Ge@Se	2.02	0.00	35		Ge@Se	2.03	0.00
12		Ge@Int	0.00	1.18	36		Ge@Int	0.00	1.25
13		B@W	0.92	0.00	37		B@W	3.03	0.17
14		B@S	0.00	0.01	38		B@S	1.01	0.00
15		B@Se	0.69	0.00	39		B@Se	0.07	0.00
16		B@Int	0.87	0.00	40		B@Int	1.10	0.00
17	$3 \times 3 \times 1$	Si@W	1.81	0.00	41	$4 \times 4 \times 1$	Si@W	1.75	0.00
18	WSSe	Si@S	0.00	0.63	42	WSSe	Si@S	0.00	0.82
19	vv bbe	Si@Se	1.90	0.00	43	wsse	Si@Se	0.00	0.95
20		Si@Int	0.00	1.49	44		Si@Int	0.00	1.49
21		Ge@W	1.85	0.00	45		Ge@W	1.92	0.07
22		Ge@S	0.00	0.38	46		Ge@S	0.00	0.58
23		Ge@Se	2.05	0.15	47		Ge@Se	2.00	0.00
24		Ge@Int	0.00	1.28	48		Ge@Int	0.00	1.34

at 3.8% DC. In the case of 2.1%, the E_{ad} of MSSe JLs, for sites 1 and 2, the E_{ad} is nearly equal (differs only by 0.08 eV). At a DC of 3.8%, the E_{ad} for sites 1 and 5 differ only by 0.10 eV and 0.09 eV, respectively.

For 2.1% Ge doping, at Mo of MoSSe, sites 3 and 4 have shown the same adsorption behavior as that of 1 and 2, which is a similar scenario as that of the B@Mo case. The H adsorption is found to be endothermic for sites 5 and 6, whereas it is exothermic for sites 1 and 2. When the doping concentration is increased, all four sites, 1, 2, 5, and 6, show exothermic behavior. In contrast to the DC of 2.1%, sites 3 and 4 show dissimilar behavior compared to sites 1 and 2 at DC 3.8%, which are found to be highly endothermic. In the case of Ge@W of WSSe, at the 3.8% DC, the H adsorption behavior follows the same trend as that of MoSSe with slightly higher E_{ad} . At 2.1% DC for the sites, 1 and 2, the H adsorption is exothermic, as that of MoSSe, and only slightly higher. Unlike in the case of MoSSe, site 6 has a lower E_{ad} compared to site 5. It means the E_{ad} is lower on the Ge when H is adsorbed on the S(Se) atomic side of MoSSe (WSSe). Similar to that at the 3.8% DC, the sites 3 and 4 show a positive E_{ad} .

Overall, for sites 1–4, the E_{ad} on MoSSe is lower compared to that of the WSSe for both DCs. This result aligns with our analysis of H adsorption energy trends in MXY (M = Mo/W; X/Y = S, Se, Te) layers, which was recently reported [70]. The reason for this is attributed to the greater electronegativity (EN) of W compared to Mo. Also, in the pristine form of the MSSe JLs, the va-

lence band maximum of WSSe lies at a higher energy than that of the MoSSe. However, this trend is not observed for sites 5 and 6, i.e., when the H atom is adsorbed on the dopant atom.

2. Doping at S site

For doping at the S site, we consider three distinct adsorption sites for H: on top of S (1), on top of Se (2), and on top of Z (3). In both the MSSe JLs, for sites 1 and 2, we observe a positive E_{ad} , and for site 3, we observe a negative E_{ad} at both the doping concentrations. The E_{ad} for WSSe is found to be slightly higher than that of MoSSe for H adsorption on sites 1 and 2, irrespective of the dopant and doping concentration. For site 3, i.e., on top of the dopant atom, E_{ad} are found to be negative in all the cases. This indicates that the Z-H bonding is stronger than the S-H or Se-H bonding. The favorable E_{ad} with less negative (>-0.45) are found for B doping at concentrations of 2.1% and 3.8%. This may be due to the locally broken structural symmetry around the dopant [71]. In all the considered cases, the E_{ad} is larger for site 2 (on top of the Se atom) and varies from 1.14 to 1.29 eV. If we compare the E_{ad} on site-3 across all cases, it is found to be less negative for B compared to Si and Ge, which may be because B acts as a p-type dopant, whereas Si and Ge are n-type dopants.

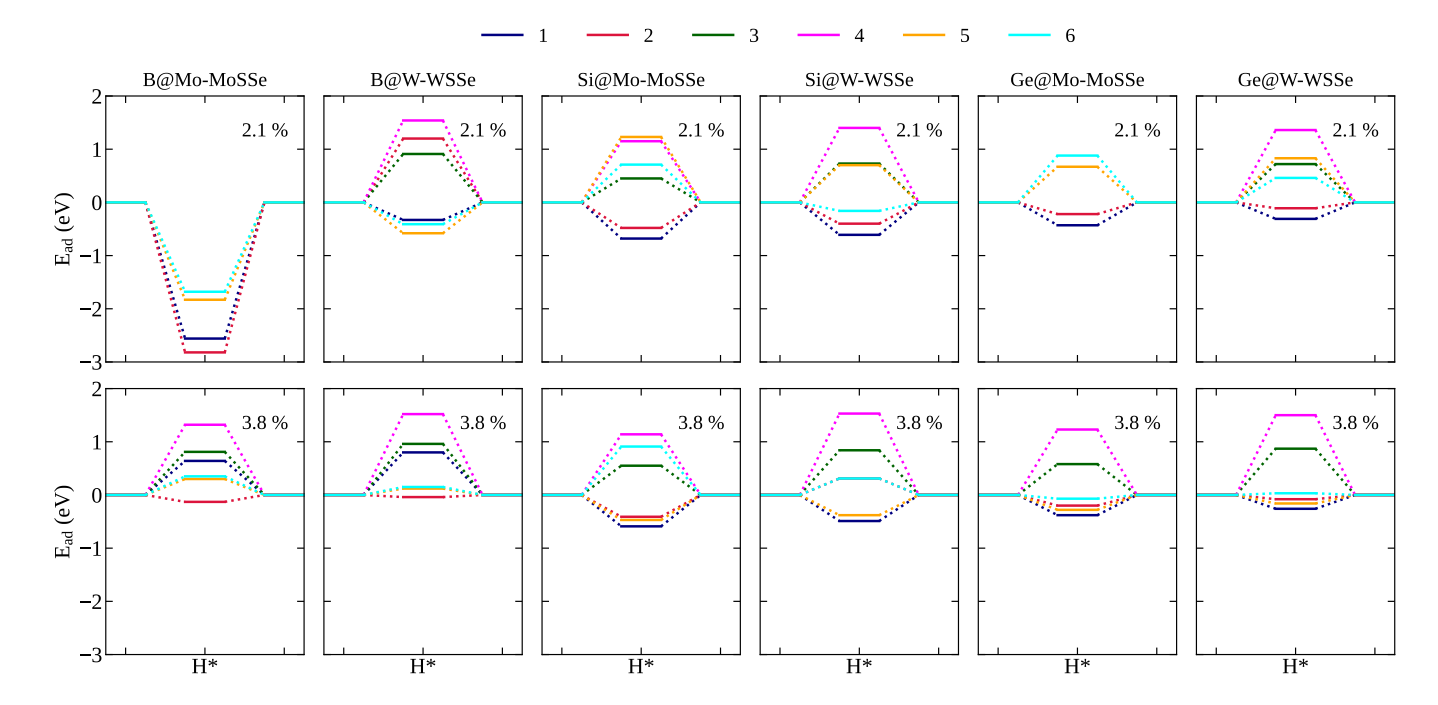


FIG. 5. Atomic H adsorption energies (E_{ad}) when the metalloid elements B, Si, and Ge are on a M site of MSSe JLs under the doping concentrations (DCs) 2.1% and 3.8%.

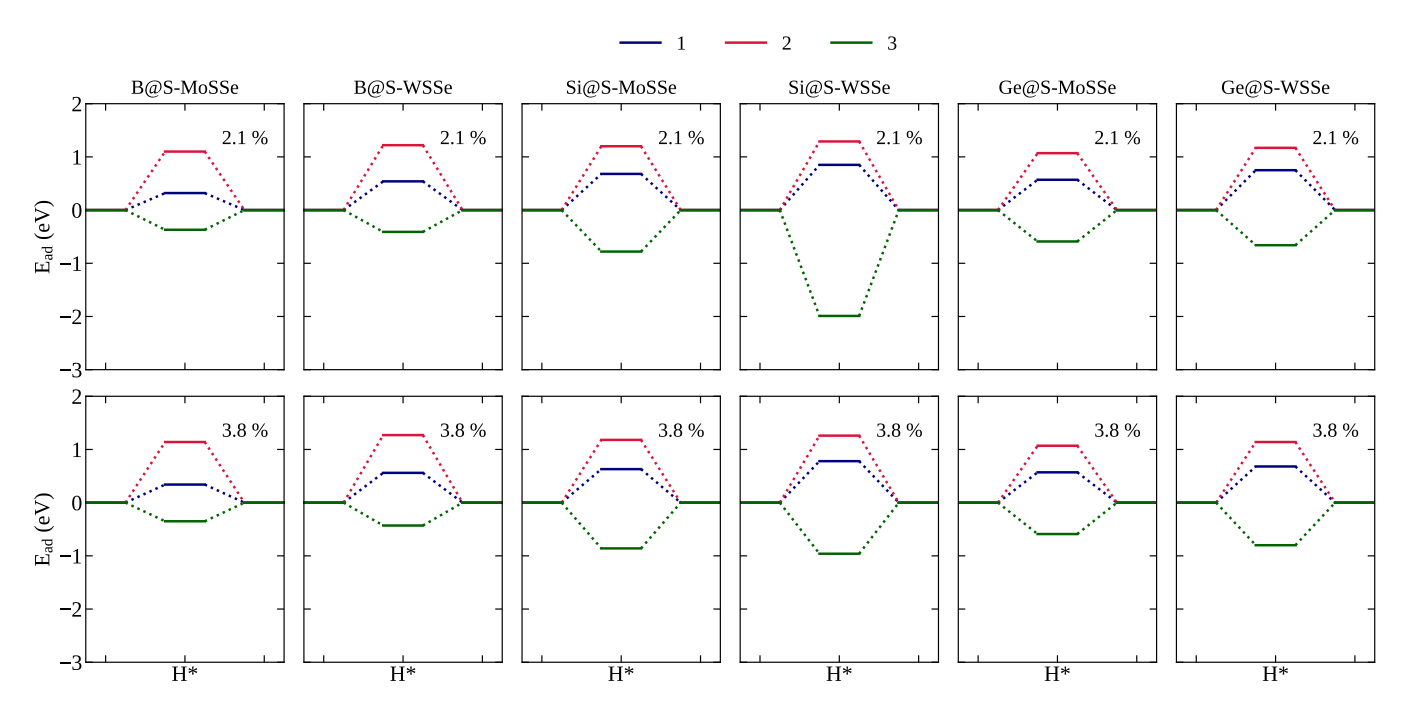


FIG. 6. Atomic H adsorption energies (E_{ad}) when the metalloid elements B, Si, and Ge are doped in place of S of MSSe JLs under the doping concentrations (DCs) 2.1% and 3.8%.

3. Dopant at Se site

The trend for H adsorption observed for the Z@Se case is similar to that observed for the Z@S case. The H adsorption reaction is found to be endothermic for sites

1 and 2, and exothermic for site 3. The E_{ad} on top of Se, i.e., for site 2, are found to be highly endothermic as compared to the other sites. For the H adsorption on site 1 the E_{ad} is slightly positive and is negligible for the cases, Ge@Se-MoSSe (2.1%), Si@Se-MoSSe(3.8%) and Ge@Se-

MoSSe (3.8%). For sites 1 and 2, the E_{ad} on MoSSe are found to be lower than those on the WSSe. This trend is similar to the case seen in pristine MSSe JLs [70]. Due to the broken symmetry near the dopant, this trend is not observed for adsorption at site 3. For the HER reaction E_{ad} should be only slightly negative. Since the Si and Ge-doped cases have larger negative adsorption energies, the B@Se cases will be more suitable for HER.

4. Dopant at the interstitial site

Finally, we study the H adsorption behavior when the dopant atom is present at an interstitial site of the MSSe JLs. Similar to the earlier two cases, Z@S and Z@Se, the H adsorption is studied at three different sites on top of the S atom (1), on top of the Se atom (2), and on the dopant atom (3). The calculated E_{ad} is as shown in Fig. 8. In the presence of the dopant at an interstitial site, the H adsorption is found to be highly endothermic for all the dopants, for all the H adsorption sites, and in both MSSe JLs at different doping concentrations. For the two cases, Ge@int of MSSe at a DC of 3.8%, convergence is not achieved during relaxation. Hence, those two cases are not shown in Fig. 8. Though the doping of Z at the interstitial site leads to n-type doping in the MSSe layers, the depleted charge has not transferred to the S or Se atomic planes and is distributed in the interstitial region, which can be observed from Fig. 3. At lower doping concentrations, similar H adsorption trends are observed for B and Ge doping. The largest E_{ad} is found for site 3, whereas the lowest E_{ad} is found for site 1. For the Si@Int, in MoSSe JL, the largest E_{ad} is found for site 3 and the lowest E_{ad} is found for site 2, with the E_{ad} for site 1 lying in between. The trend is not the same for Si@Int in the WSSe JL. In WSSe JL, the largest E_{ad} is found for site 2 and the smallest is found for site 3, with the E_{ad} of site 1 lying in between. At 3.8% DC, the B and Si doping at the interstitial site are showing a similar trend with the larger E_{ad} corresponding to site 2, and the lowest E_{ad} is observed for site 3, with site 2 lying in between.

E. Workflow for the ML predictions

Due to the peculiar properties shown by the JLs, the number of studies on these JLs is increasing year by year. Due to the lack of available datasets containing H atom adsorption energies in the presence of dopants, this study will be beneficial for researchers exploring 2D photocatalysts for clean H₂ production. Using the DFT generated, we develop an ML model entirely based on the fundamental elemental properties of the atoms. The schematic illustrating the workflow is depicted in Fig. 9. The step-by-step procedure we follow for the implementation of the ML model is as follows:

- 1. In the first step, we extract the DFT calculated H atom adsorption energies in the presence of the metallolid dopants B, Si, and Ge under two distinct doping concentrations. All the above-discussed distinct sites for H atom adsorption are considered for each dopant. Thus, we ended up with a total of 178 data points.
- 2. In the second step, we identify the elemental features of the atoms that characterize the dopant and its location. The chemical properties of the elements have already been successfully utilized in predicting various physical and chemical properties of materials. The details of the feature selection are discussed in IIIF 2
- 3. In the third step, we engineer the features into a better representable form for training the ML model. For this purpose, we utilize the dimensionality reduction technique of PCA, which not only reduces the dimension of the feature space but also yields independent features, known as principal components (PCs), that can be used as descriptors for the ML model.
- 4. In the fourth step, we provide the PCs resulting from PCA as input and select the ML model for training. In this scenario, we use the multilayer perceptron regression model.
- 5. In the fifth step, we tune various hyperparameters such as the number of hidden layers, the number of neurons in each hidden layer, the type of activation function, the initial learning rate, and the number of epochs till the optimal performance on the training data has been achieved.
- 6. In the final step, with the identified best hyperparameter set, we test the performance of the model by calculating the metrics RMSE and R². The robustness of the model is confirmed by calculating the metrics with 10 distinct random numbers.

F. Neural network model for predicting dopant adsorption energies

1. Dataset preparation

Based on the discussions above regarding the DFT results, we have a total of 178 data points representing the \mathbf{E}_{ad} in the presence of three metalloid dopants, B, Si, and Ge, in the MSSe JLs. Two dopant concentrations are considered by the selection of the $3\times3\times1$ and $4\times4\times1$ supercells. Supercells, with dopant sites Z@Mo, Z@S, Z@Se, and Z@Int. For each dopant, we have $60~\mathbf{E}_{ad}$ data points for H adsorption on different sites as shown in Fig. 1(b). Due to the structural distortion and convergence issues, we exclude two data points. The two

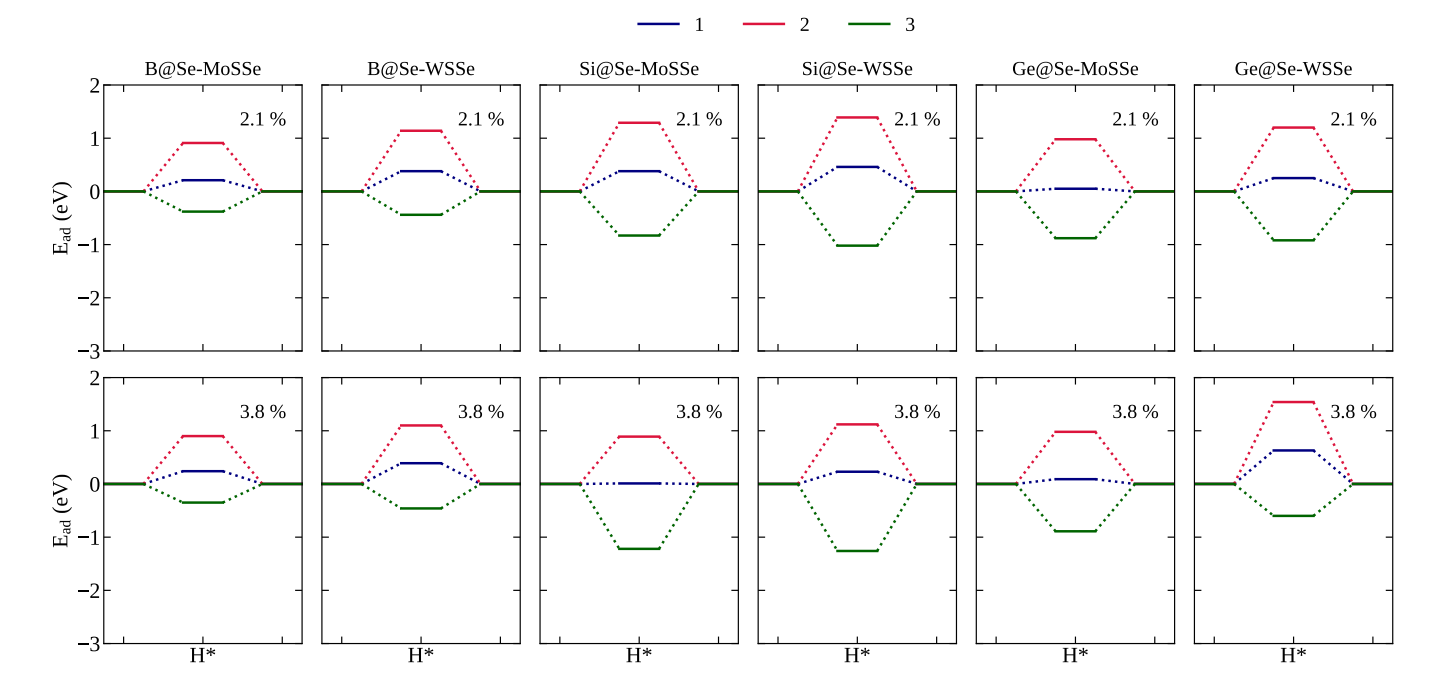


FIG. 7. Atomic H adsorption energies (E_{ad}) when the metalloid elements B, Si, and Ge are doped on a Se site of MSSe JLs under the doping concentrations (DCs) 2.1% and 3.8%.

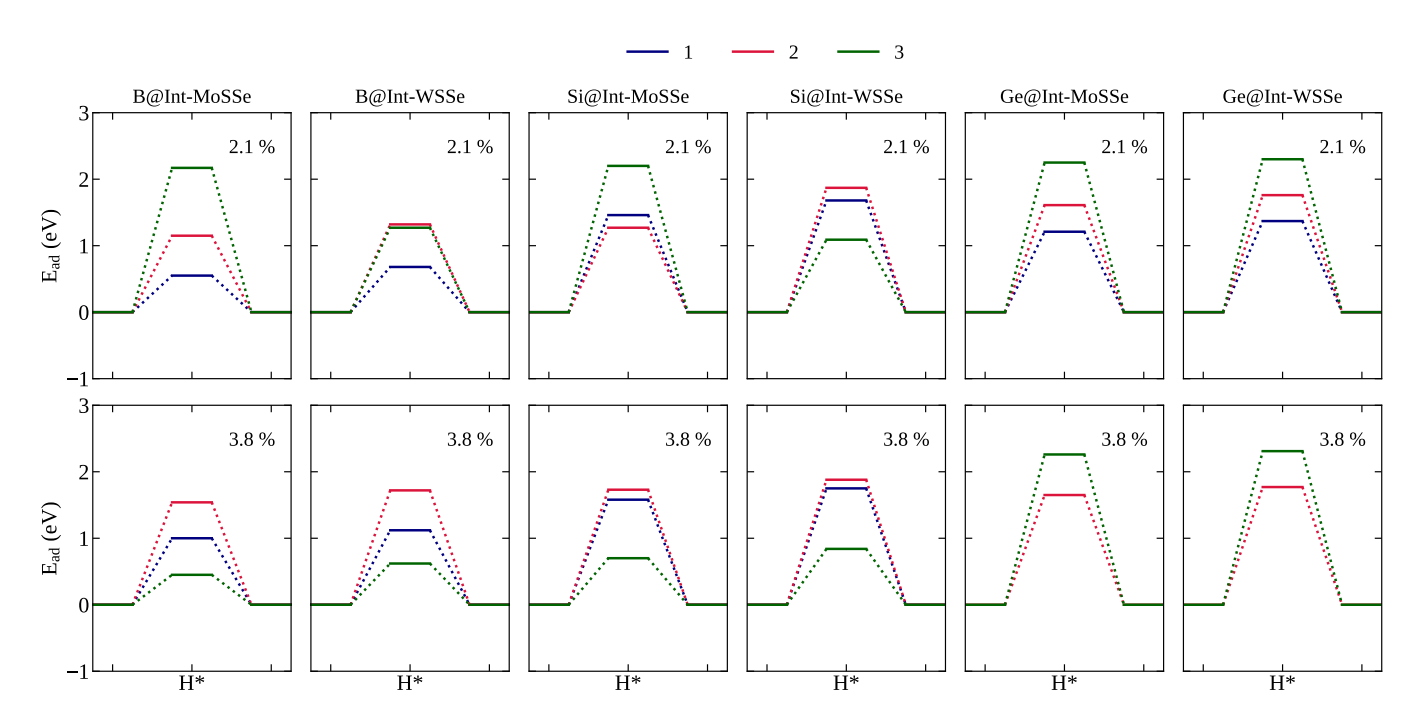


FIG. 8. Atomic H adsorption energies (E_{ad}) when the metalloid elements B, Si, and Ge are doped at an interstitial of MSSe JLs under the doping concentrations (DCs) 2.1% and 3.8%.

excluded points are when H is adsorbed on the S atom of MSSe JLs in the presence of the Ge@Int at DC 3.8%. Thus, finally, we have a total of 178 data points. The details of the E_{ad} dataset are given in STable 1. However, the size of the available data is comparatively small to

build a robust ML model. Thus, we adopt the data augmentation technique to expand the dataset by generating slightly deviated copies of the original data, which will be discussed in the *Data augmentation* section. The use of data augmentation not only increases the size of the

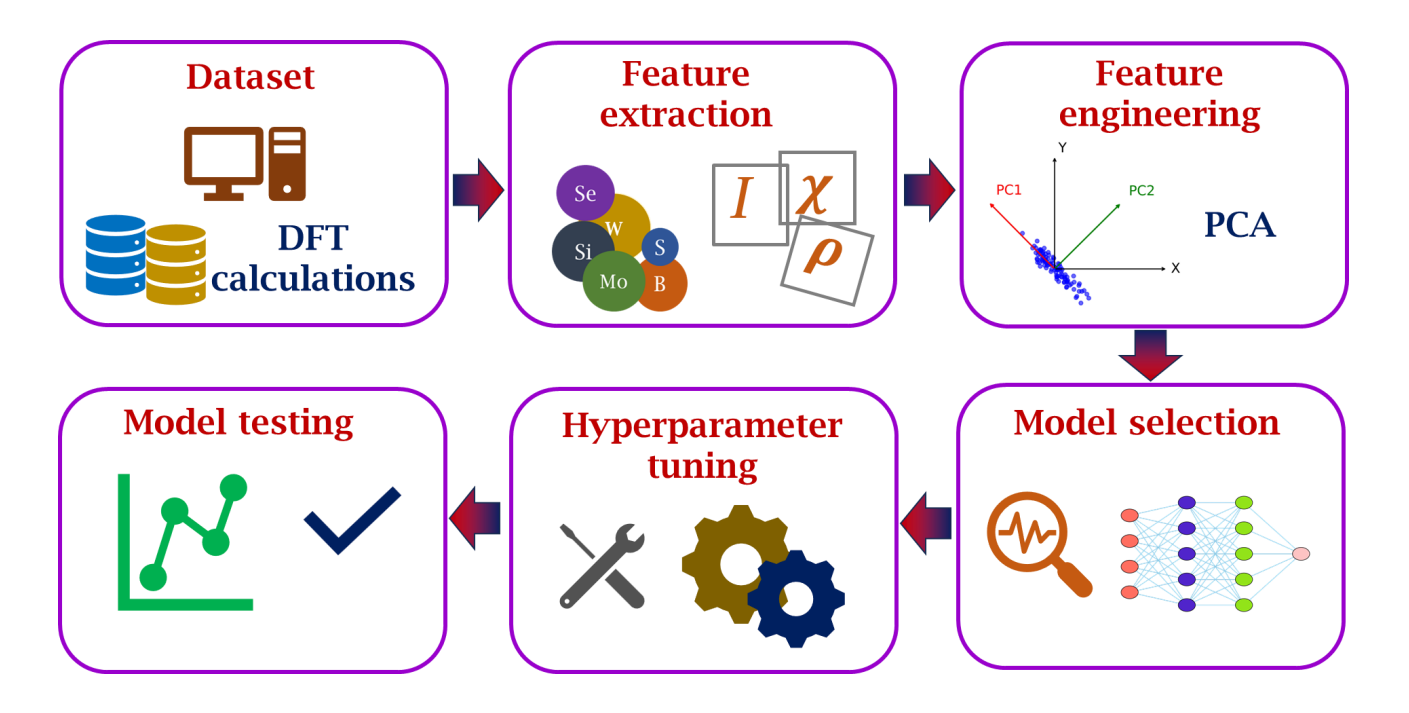


FIG. 9. The schematic illustrating the workflow followed to predict the H atom adsorption energies in the presence of substitutional and interstitial dopants B, Si, and Ge in MSSe Janus layers.

data, but it also makes the model more generalizable and addresses data imbalance. Using the augmented dataset, we develop an ML model to predict E_{ad} . In the following sections, we discuss the details of feature selection and the feature engineering techniques.

2. Feature selection and physical importance

From the DFT analysis, it is clear that E_{ad} strongly depends on the surface of adsorption, charge distribution, dopant site, and the adsorption site. To train any ML model, the first step is to identify the most appropriate, accurate features that best describe the data. Herein, we design the descriptors based on the elemental features of the species and two less expensive features calculated from the DFT. The identification of the features is done such that the chosen features should distinguish the JLs, dopant elements, and the H adsorption site. The 23 primary elemental features, along with their notation and physical importance, are listed in Table II.

The identified chemical properties of the elements n_H and n_d give information about the hydrogen coverage and doping concentration in the MSSe JLs. The features, $\delta \chi$, δv , and δI , characterizes the modified charge distribution, bonding and electron transfer with the substitution of the dopant. The features $\sum r^a$ and $\sum r^c$ pin the atom on top of which H adsorption occurs and also describes about the H bonding character to the adsorption site. To distinguish between distinct H adsorption sites on the MSSe JLs, we include the first and sec-

ond nearest neighbours with respect to the adsorbed H atom. To distinguish between the first and second nearest neighbours, we use a tolerance factor of 0.05Å. The $r_{1\mathrm{nn}}^{a}$ feature gives information about the atom on top of which the H atom is adsorbed. This means that it provides details on whether the H is adsorbed on S/Se or the dopant Z. Thus, based on the considered sites, one of S/Se/B/Si/Ge will always be the first nearest neighbour. The second-nearest neighbour features play a key role in distinguishing the H adsorption site more clearly. First nearest neighbour features provide only the information of the atom on which H is adsorbed, without distinguishing between all the considered adsorption sites. For example, if we consider the cases of Si@S and Ge@S in MoSSe with H adsorption on the S surface, the first nearest neighbours are the same for both cases. The second nearest neighbour features will give the change in the chemical environment for both cases. Thus, we include the second nearest neighbour features $(N_{2\text{nn}}, N_{2\text{nn}}^{\text{M}}, N_{2\text{nn}}^{\text{S}}, N_{2\text{nn}}^{\text{N}}, N_{2\text{nn}}^{\text{S}}, N_{2\text{nn}}^{\text{N}}, N_{2\text{nn}}^{\text{S}}, N_{2\text{nn}}^{\text{S}}$ is given in Table II. To make a distinction between the MSSe JLs, we use the chemical potential of the Mo and W atom μ^M as a feature, which is calculated using DFT with a bulk system of Mo/W as a reference. To differentiate between the dopants, we also include the dopant chemical potential μ^Z as an additional feature. However, the use of too many features in training the ML model results in a significant increase in computational cost and also leads to overfitting. Thus, choosing the more ap-

TABLE II. The notation and physical importance of identified elemental features.

Feature Name	Symbol	Physical Importance
Hydrogen concentration	$n_{ m H}$	Includes supercell dependent H coverage
Doping concentration	$n_{ m d}$	Represents the amount of doping introduced into the system.
Pauling electronegativity difference (elimi-	$\delta \chi$	Captures the charge transfer variation due to introduction of the
nated atom vs. dopant)		dopant.
Valency difference (eliminated atom vs.	δv	Describes the bonding character upon the introduction of the
dopant)		dopant
Ionization energy difference (eliminated atom vs. dopant)	δI	Reflects the charge transfer from/to the dopant
Sum of atomic radii of H and adsorption atom	$\sum r^a$	Indicates the H adsorption site and characterizes the bonding
Sum of covalent radii of H and adsorption atom	$\sum r^c$	Characterizes the H bonding with the atom on top of which H is adsorbed
Atomic radius of first nearest neighbour	$r_{1\mathrm{nn}}^{a}$	Provides information about the nearest atom influencing H adsorption.
Number of second nearest neighbours	$N_{ m 2nn}$	Captures the local environment around the H-adsorbed site.
Number of metal atoms in SNNs	$N_{ m 2nn}^{ m M}$	Determines the role of metal atoms in the adsorption behavior.
Number of S atoms in SNNs	$N_{ m 2nn}^{ m S}$	Determines the role of S atoms in the adsorption behavior.
Number of Se atoms in SNNs	$N_{ m 2nn}^{ m Se}$	Determines the role of Se atoms in the adsorption behavior.
Number of dopant atoms in SNNs	$N_{ m 2nn}^{ m Z}$	Reflects the influence of dopant atoms in the SNNs on H adsorption.
Average atomic radius of SNNs	$ar{r}_{2 ext{nn}}^a$	Characterizes the local environment around the H-adsorption site
Average covalent radius of SNNs	$ar{r}_{2 ext{nn}}^c$	Characterizes the local environment around the H-adsorption site
Average electronegativity of SNNs	$ar{\chi}_{2\mathrm{nn}}$	Characterizes the local chemical environment around the H-adsorption site
Average ionization energy of SNNs	$ar{I}_{2\mathrm{nn}}$	Characterizes the local environment around the H-adsorption site
Sum of atomic radii of SNNs	$\sum r_{2 ext{nn}}^a$	Describes the size-dependent nature of the SNN environment
Sum of covalent radii of SNNs	$\overline{\sum} r^c_{2{ m nn}}$	Describes the bonding characteristics of the SNN environment
Sum of electronegativities of SNNs	$\sum \chi_{2\mathrm{nn}}$	Reflects the collective electron-attracting ability of the SNN atoms.
Sum of ionization energies of SNNs	$\sum I_{2\mathrm{nn}}$	Reflects the collective ionization energy of SNN atoms influencing H adsorption.
Chemical potential of M	μ^M	Distinguishes between MSSe monolayers.
Chemical potential of dopant	μ^X	Distinguishes the dopants B, Si, and Ge.

propriate and independent features is always preferred. For this purpose, we utilize the feature engineering and dimensionality reduction technique of PCA.

3. Principal component analysis

Principal component analysis is a dimensionality reduction method that projects the n-dimensional feature vectors in the original feature space into principal components(PCs), which are the linear combination of the original features in a lower-dimensional space [72]. The eigenvectors of the covariance matrix of the original data produce PCs. Intuitively, they give the directions of maximum variance, and the corresponding eigenvalues give the variance values. The eigenvalues are sorted in decreasing order of their variances, and the top k eigenvectors (k is less than or equal to n) that accommodate most of the variance (like 95%, 98%, or 99% as a parameter) in the data are chosen. The points in the original space are then projected onto the k-dimensional space spanned by the k eigenvectors. As such, final predictions can be performed in a lower k-dimensional space instead of a higher n-dimensional space, thereby reducing computational complexity. Since the PCA-generated PCs are orthogonal to each other, they act as the best features for the ML model.

By performing PCA on the original 23 features with a variance recovery of 98% we ended up with 11 PCs, which are independent of each other and hence each PC captures the unique information from the data. Due to the reduced dimensionality, the PCs hold the hidden correlations in the original data [73]. The percentage of variance explained by each of the PC is given in Fig. 10(b). The first PC (PC1) covers the highest amount of variance in the data, i.e., 41.46%, and the second PC(PC2) covers an amount of 13.49%. To understand the variance among all the features, we have analyzed the loading plot for PC1, which is given in Fig. 10(a). Loadings are defined as the contribution of each variable to the PC. The loadings plot for PC2 is also analyzed and is given in SFig. 9. With only two PCs, nearly 55% of the variance is retained. The contribution of each of the features can also be observed from Eq. 3 and 4. For PC1, the most important features are N_{2nn} , N_{2nn}^M , $\bar{r}^a{}_{2nn}$, $\bar{r}^c{}_{2nn}$, $\bar{\chi}_{2nn}$, \bar{I}_{2nn} , $\sum r_{2nn}^a$, $\sum \chi_{2nn}$ and $\sum I_{2nn}$. This suggests that the SNN features play a crucial role in predicting E_{ad} , which characterizes the local bonding character and charge distri-

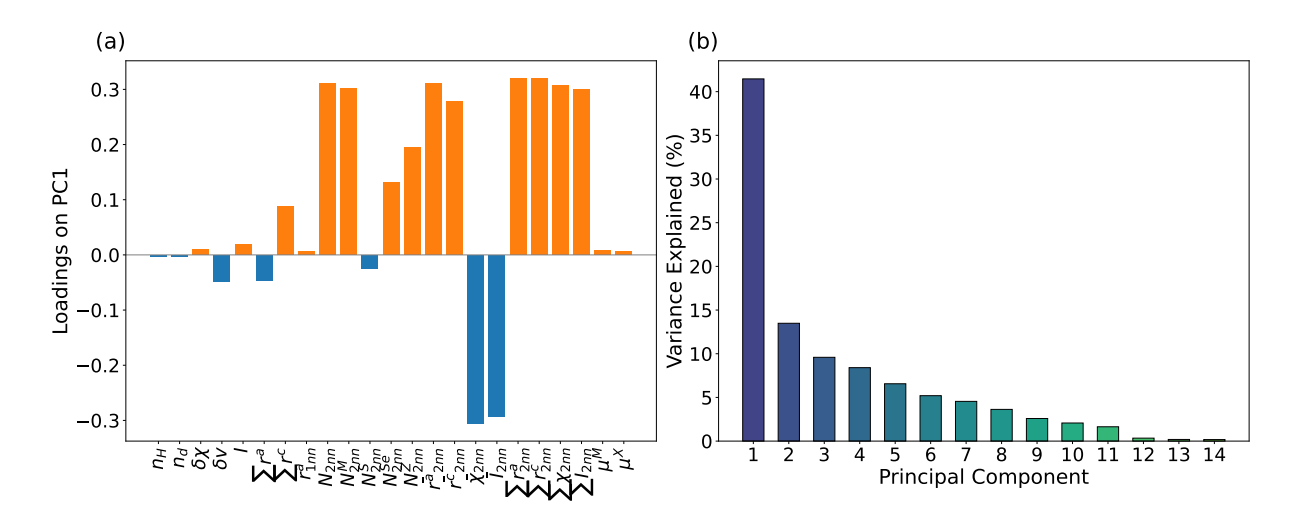


FIG. 10. (a) Loadings plot representing the contribution of each feature in obtaining the PC1 and (b) The variance (%) explained by each of the principal components.

bution. For PC2, the key features are $\sum r^a$, $\sum r^c$, N_{2nn}^S and N_{2nn}^{Se} . The sum of atomic (covalent) radii of H and the atom on which H is being adsorbed well describes the H-host atom bonding, and N_{2nn}^S and N_{2nn}^{Se} represent the presence of S/Se in the neighbourhood of H, and hence are important features influencing E_{ad} .

$$PC1 = -0.0028 n_{H} - 0.0028 n_{d} + 0.0105 \delta \chi - 0.0480 \delta v$$

$$+ 0.0184 I - 0.0457 \sum_{n} r^{a} + 0.0885 \sum_{n} r^{c}$$

$$+ 0.0067 r_{1nn}^{a} + 0.3116 N_{2nn} + 0.3023 N_{2nn}^{M}$$

$$- 0.0242 N_{2nn}^{S} + 0.1313 N_{2nn}^{Se} + 0.1941 N_{2nn}^{Z}$$

$$+ 0.3105 \bar{r}_{2nn}^{a} + 0.2785 \bar{r}_{2nn}^{c} - 0.3062 \bar{\chi}_{2nn}$$

$$- 0.2924 \bar{I}_{2nn} + 0.3205 \sum_{n} r_{2nn}^{a} + 0.3192 \sum_{n} r_{2nn}^{c}$$

$$+ 0.3079 \sum_{n} \chi_{2nn}^{c} + 0.3009 \sum_{n} I_{2nn}^{c} + 0.0078 \mu^{M}$$

$$+ 0.0061 \mu^{X}$$
(3)

$$PC2 = -0.0289 \, n_H - 0.0290 \, n_d - 0.0687 \, \delta \chi + 0.0119 \, \delta v$$

$$-0.0660 \, I - 0.4579 \sum r^a - 0.4237 \sum r^c$$

$$-0.0288 \, r_{1nn}^a + 0.1105 \, N_{2nn} + 0.0884 \, N_{2nn}^M$$

$$+0.4794 \, N_{2nn}^S - 0.4379 \, N_{2nn}^{Se} + 0.1114 \, N_{2nn}^Z$$

$$-0.0747 \, \bar{r}_{2nn}^a - 0.2099 \, \bar{r}_{2nn}^c + 0.1022 \, \bar{\chi}_{2nn}$$

$$-0.0342 \, \bar{I}_{2nn} + 0.0507 \sum r_{2nn}^a + 0.0475 \sum r_{2nn}^c$$

$$+0.1135 \sum \chi_{2nn} + 0.1439 \sum I_{2nn} + 0.0024 \, \mu^M$$

$$-0.2131 \, \mu^X$$

$$(4)$$

4. Multilayer perceptron regression

Using the 11 PCs as features, we train a neural network model based on multi-layer perceptrons [74, 75]. The training and testing data are divided into ratios of 70:30 and 80:20. We perform various experiments with the model to obtain the best prediction. For this, we examine the neural network model with the optimization techniques Adam [76], Limited-memory Broyden-Fletcher-Goldfarb-Shanno (LBFGS) [77], and stochastic gradient descent (SGD) [78] in combination with the activation functions rectifying linear unit (ReLU), tanh, and sigmoid function.

The key hyperparameters for the neural network model are the optimization method, the activation function, and the architecture of the hidden layers. Of the three optimization methods available in the sklearn package [79], LBFGS and Adam, in combination with the ReLU activation function, yield good performance for our data. Thus, we test the performance of the model with this combination. We vary the number of hidden layers and the number of neurons in each of the hidden layers and test the performance of the model. The number of hidden layers is varied from 1 to 3, and their depth is varied in multiples of 10 from a minimum of 10 to 100. To assess the robustness of the neural network for a fixed set of all hyperparameters, we use 10 distinct random seeds and observe the performance of the model each time by calculating the root mean squared error (RMSE) and the coefficient of determination (R^2) . The standard deviation of these metrics for 10 distinct random seeds quantifies the robustness of the model.

When we analyze all 178 data points and evaluate the performance of the model with different hyperparameter sets, we find that data points related to 2.1% B@Mo doping appear as outliers in the predicted data, which leads to reduced performance and stability of the model.

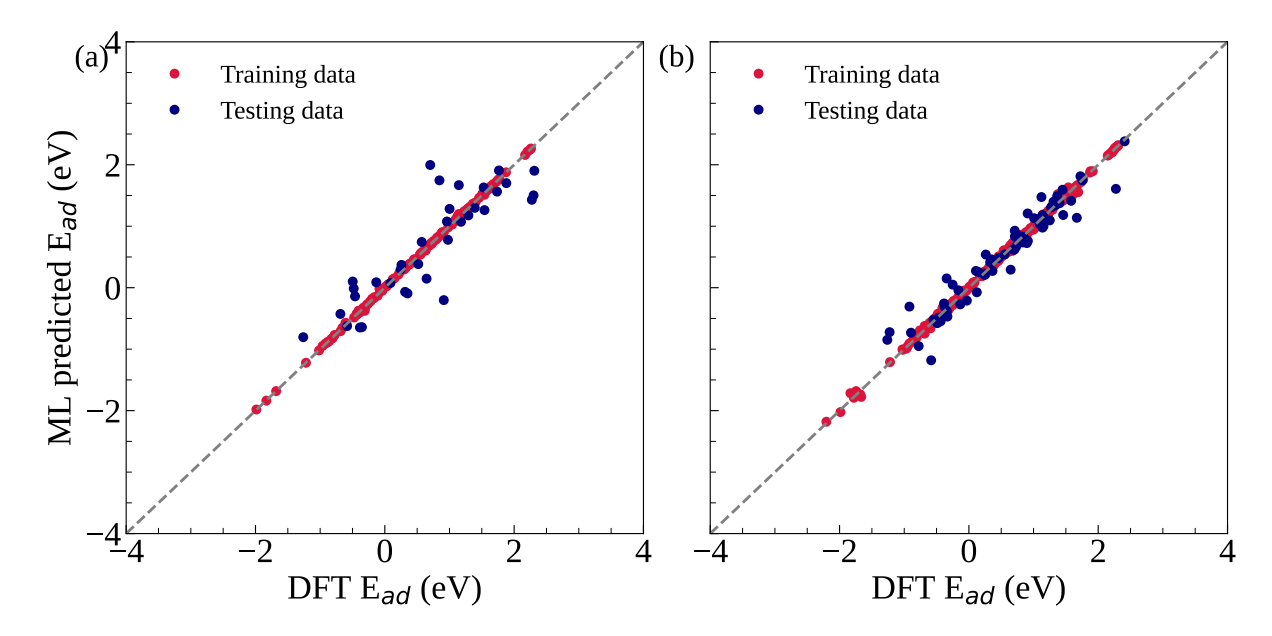


FIG. 11. The DFT calculated versus ML predicted E_{ad} with the principal components as the features (a) without and (d) with data augmentation, respectively. The performances reported here are the average performance on the test data achieved by using the 10 distinct random seeds.

The parity plot comparing DFT and ML predicted Ead for this case is shown in SFig. 10. The highest stability achieved for this case is 0.1412, which is quite high. The metrics RMSE and R² for the testing data are found to be 0.5928 eV and 0.57, respectively. This is due to the significant deviation of Ead values for 2.1% B@Mo doping from all the other cases (see Fig. 5). Thus, we exclude the four data points corresponding to the B@Mo doping under 2.1% doping concentration and consider the remaining 174 data points for our study. We train the neural network using 11 principal components as input, and the performance of the model is evaluated after hyperparameter tuning. From our experimentation, we found that the 80:20 training and testing data split ratio is the best compared to the 70:30 split, as the model is well-trained with a large number of data points in the 80:20 split case, resulting in the best performance. The optimization technique LBFGS, in combination with the ReLU activation function, yields the best prediction compared to other optimizer and activation function combinations. The calculated metrics RMSE and R² for the testing (training) data are 0.4322 eV (0.0110 eV) and 0.75 (0.99), respectively. The DFT versus ML predicted E_{ad} parity plot is given in Fig 11(a). The robustness of the model is confirmed by measuring the standard deviation of the testing data R² with 10 distinct random seeds. The observed standard deviation is 0.0881, which indicates the stability of the model. We also check the performance of the model with the Adam optimization technique. The Adam optimizer with the ReLU activation function yields R^2 of 0.72 (RMSE = 0.7244 eV) on the test data, which is lower compared to the LBFGS optimization technique. The standard deviation of 0.0995

is slightly higher compared to that with LBFGS. However, the performance of the model is limited to 75% with either of the optimization methods due to the comparatively smaller size of the dataset. To improve the accuracy of the model and data imbalances, we employ the technique of data augmentation, which artificially generates data points in the neighbourhood of the original data points.

5. Data augmentation

We increase the dataset size by utilizing a data augmentation technique known as the Synthetic Minority Over-Sampling Technique for Regression (SMOTER) [80]. The SMOTER technique generates the synthetic data points using the K-Nearest Neighbours (KNN) algorithm. We double the size of the dataset to 348 and analyze the performance of the model on the combined dataset of original data points and synthetic data points. Similar to the earlier case, when PCA with 98% variance coverage is implemented on the combined dataset, 11 principal components are obtained. We use these 11 principal components as input features and train the neural network. With data augmentation, its performance improves significantly, as indicated by the testing (training) data metrics: RMSE 0.2583 eV (0.0273 eV) and R^2 0.90 (0.99), respectively. The DFT versus ML predicted scatter plot for the augmented data is shown in Fig. 11(b). The optimized hyperparameters for the case of augmented data are an 80:20 training and testing data split, LBFGS optimizer with a ReLU activation function, and two hidden layers with 90 neurons each. We calculate the standard deviation of R² for the testing data, obtained using 10 distinct random seeds. The standard deviation is found to be 0.0387, indicating the robustness of the model. The parity plot of DFT versus ML predicted E_{ad} for the MLPR model when all the 23 original features are used as descriptors is provided in SFig. 11 (a) and (b) for the original and augmented data, respectively. The performance of the neural network on the augmented data suggests that the proposed procedure of feature selection and feature engineering is beneficial for accurately predicting E_{ad} using larger datasets. The performance of the model is also examined with the Adam optimizer, with the three hidden layers and 80 neurons in each layer. The metrics RMSE and R² for the testing data are found to be 0.3028 eV and 0.88, respectively. To understand the effectiveness of the training process with Adam, we calculate the training and validation losses for each epoch using the Adam optimizer, as shown in SFig. 12(a). The DFT versus ML predicted scatterplot is given in SFig. 12(b). For validation purposes, 10% (28 data points) of the training data is being used. The given curves suggest that the model is neither overfitting nor underfitting, as indicated by the gradual decrease in both the training and validation losses. Thus, the developed model is robust and can predict the E_{ad} using elemental information without requiring DFT calculations for feature extraction.

IV. CONCLUSION

In summary, we systematically investigate the adsorption of H atoms on MSSe JLs in the presence of metalloid dopants B, Si, and Ge using DFT calculations. The doping concentration and hydrogen coverage are taken into account by considering the supercells of sizes $4\times4\times1$ and $3\times3\times1$ representing the concentration 2.1% and 3.8%, respectively. For the introduction of the dopants into the MSSe JLs, three atomic sites and one interstitial site have been selected. The calculated binding energies of the dopants suggested that the three metalloids are favorable for doping. The electronic structure calculations for the doped systems have revealed the spin-polarization and reduced band gaps. From DOS, it is found that the spin polarization mainly originated from the partially filled d orbitals of Mo/W atoms. It is observed that the MSSe layers undergo a transition from semiconducting

to half-metallic and metallic phases, depending on the type of dopant and doping site. Due to the charge redistribution around the dopant, several sites have been activated for H atom adsorption. In certain cases, the H adsorption process on the MSSe JLs is found to be spontaneous with the introduction of dopants. In contrast, in the pristine form, it has resulted in a positive adsorption energy. However, interstitial site doping does not lead to spontaneous H adsorption, and the process remains exothermic. Overall, from the H adsorption energies, it is found that B doping at S/Se atomic planes is favourable for HER, as it results in less negative \mathbf{E}_{ad} , satisfying the HER criteria.

Using the total of 178 E_{ad} data points, we have developed an ML model that predicts \mathbf{E}_{ad} using the 23 chemical properties of the atoms involved in the structure. By performing the PCA, the dimension of the feature space is reduced from 23 to 11. With the 11 principal components finally obtained from PCA, we trained a multilayer perceptron regression model and achieved an R² of 0.75 on the testing data. The stability of the model is characterized by the calculation of the standard deviation, which is found to be 0.0881, obtained by varying the random seed. Due to the comparatively small size of the data set, the accuracy of the model is limited to 75%. To increase the number of training data points and accuracy, we employed the data augmentation technique SMOTER, which doubled the number of data points. With the combined dataset of original and artificial data points, the accuracy of the model is increased to 90% with a stability of 0.0387. Thus, the ML model based on fundamental atomic properties is the best model for predicting atomic H adsorption energies in monolayers with impurities.

ACKNOWLEDGMENTS

G.T and D.M acknowledge funding by the DST-SERB within the project CRG/2022/006778. D.M thanks the Department of Information Services and Computing at Helmholtz-Zentrum Dresden-Rossendorf for providing extensive computational facilities. This work was in part supported by the Center for Advanced Systems Understanding (CASUS), which is financed by Germany's Federal Ministry of Research, Technology and Space (BMFTR) and by the Saxon State government out of the State budget approved by the Saxon State Parliament.

R. Yang, Y. Fan, Y. Zhang, L. Mei, R. Zhu, J. Qin, J. Hu, Z. Chen, Y. Hau Ng, D. Voiry, S. Li, Q. Lu, Q. Wang, J. C. Yu, and Z. Zeng, 2D Transition Metal Dichalcogenides for Photocatalysis, Angewandte Chemie International Edition 62, e202218016 (2023).

^[2] S. Manzeli, D. Ovchinnikov, D. Pasquier, O. V. Yazyev, and A. Kis, 2D transition metal dichalcogenides, Nat Rev

Mater 2, 17033 (2017).

^[3] K. S. Novoselov, A. K. Geim, S. V. Morozov, D. Jiang, Y. Zhang, S. V. Dubonos, I. V. Grigorieva, and A. A. Firsov, Electric Field Effect in Atomically Thin Carbon Films, Science 306, 666 (2004).

^[4] X. Duan and H. Zhang, Introduction: Two-Dimensional Layered Transition Metal Dichalcogenides, Chemical Re-

- views 124, 10619 (2024).
- [5] C. Wang, F. Yang, and Y. Gao, The highly-efficient light-emitting diodes based on transition metal dichalcogenides: from architecture to performance, Nanoscale Adv. 2, 4323 (2020).
- [6] Z. Zhou, J. Lv, C. Tan, L. Yang, and Z. Wang, Emerging Frontiers of 2D Transition Metal Dichalcogenides in Photovoltaics Solar Cell, Adv. Funct. Mater. 34, 2316175 (2024).
- [7] P. Bora, S. Kumar, and D. Sinha, 2D transition metal dichalcogenides for efficient hydrogen generation, Materials Today Sustainability 27, 100914 (2024).
- [8] A. Eftekhari, Tungsten dichalcogenides (WS2, WSe2, and WTe2): materials chemistry and applications, J. Mater. Chem. A 5, 18299 (2017).
- [9] T. Hu, F. Jia, G. Zhao, J. Wu, A. Stroppa, and W. Ren, Intrinsic and anisotropic Rashba spin splitting in Janus transition-metal dichalcogenide monolayers, Phys. Rev. B 97, 235404 (2018).
- [10] A. Jain and C. Bera, Rashba spin-splitting and spin Hall effect in Janus monolayers Sb2XSX' (X, X'= S, Se, or Te; $X \neq X$ '), Journal of Applied Physics **135**, 114302 (2024).
- [11] Y. Wei, X. Xu, S. Wang, W. Li, and Y. Jiang, Second harmonic generation in Janus MoSSe a monolayer and stacked bulk with vertical asymmetry, Phys. Chem. Chem. Phys. 21, 21022 (2019).
- [12] S.-Q. LI, C. He, H. Liu, L. Zhao, X. Xu, M. Chen, L. Wang, J. Zhao, and J. Gao, Dramatically Enhanced Second Harmonic Generation in Janus Group-III Chalcogenide Monolayers, Advanced Optical Materials 10, 2200076 (2022).
- [13] T. Gorkan, J. Das, J. Kapeghian, M. Akram, J. V. Barth, S. Tongay, E. Akturk, O. Erten, and A. S. Botana, Skyrmion formation in Ni-based Janus dihalide monolayers: Interplay between magnetic frustration and Dzyaloshinskii-Moriya interaction, Phys. Rev. Mater. 7, 054006 (2023).
- [14] W. Pan, S. Ji, and Z. Xu, Strain-induced intrinsic antiferromagnetic skyrmions in two-dimensional Janus magnets, Phys. Rev. B 110, 144408 (2024).
- [15] T. Zheng, Y.-C. Lin, Y. Yu, P. Valencia-Acuna, A. A. Puretzky, R. Torsi, C. Liu, I. N. Ivanov, G. Duscher, D. B. Geohegan, Z. Ni, K. Xiao, and H. Zhao, Excitonic Dynamics in Janus MoSSe and WSSe Monolayers, Nano Letters 21, 931 (2021).
- [16] A. E. Sudheer, A. Kumar, G. Tejaswini, M. Vallinayagam, M. Posselt, M. Zschornak, C. Kamal, and D. Murali, A first principles study on the stability and electronic and optical properties of 2D SbXY (X = Se/Te and Y = I/Br) Janus layers, Phys. Chem. Chem. Phys. 26, 29371 (2024).
- [17] A. E. Sudheer, G. Tejaswini, M. Posselt, and D. Murali, First principles investigation on structural and optoelectronic properties of newly designed Janus lead halides PbXY (X, Y = F, Cl, Br, I), Computational Materials Science 243, 113123 (2024).
- [18] Patel, Abhishek and Singh, Deobrat and Sonvane, Yogesh and Thakor, P. B. and Ahuja, Rajeev, High thermoelectric performance in two-dimensional janus monolayer material ws-x (x = se and te), ACS Applied Materials & Interfaces 12, 46212 (2020).
- [19] M. Vallinayagam, M. Posselt, and S. Chandra, Electronic structure and thermoelectric properties of Mobased dichalcogenide monolayers locally and randomly

- modified by substitutional atom, RSC Adv. **10**, 43035 (2020).
- [20] D. H. Ozbey, M. J. Varjovi, G. O. Sarg m, H. Sevinçli, and E. Durgun, Structural, electronic, vibrational, and thermoelectric properties of Janus $Ge_2PX(X = N, As, Sb, andBi)$ monolayers, Phys. Rev. B **110**, 035411 (2024).
- [21] M. Vallinayagam, A. Kumar, A. E. Sudheer, G. Te-jaswini, M. Posselt, C. Kamal, M. Zschornak, and D. Murali, Thermoelectric properties of Lead halide Janus layers A theoretical investigatio (2025), arXiv:2509.16992 [cond-mat.mtrl-sci].
- [22] M. Yagmurcukardes, Y. Qin, S. Ozen, M. Sayyad, F. M. Peeters, S. Tongay, and H. Sahin, Quantum properties and applications of 2D Janus crystals and their superlattices, Appl. Phys. Rev. 7, 011311 (2020).
- [23] L. Zhang, Y. Liu, Z. Xu, and G. Gao, Electronic phase transition, perpendicular magnetic anisotropy and high Curie temperature in Janus FeClF, 2D Materials 10, 045005 (2023).
- [24] L. Ju, M. Bie, J. Shang, X. Tang, and L. Kou, Janus transition metal dichalcogenides: a superior platform for photocatalytic water splitting, J. Phys. Mater. 3, 022004 (2020).
- [25] M. Vallinayagam, A. E. Sudheer, S. A. Aravindh, D. Murali, N. Raja, R. Katta, M. Posselt, and M. Zschornak, Novel Metalless Chalcogen-Based Janus Layers: A Density Functional Theory Study, The Journal of Physical Chemistry C 127, 17029 (2023).
- [26] L. Ju, M. Bie, X. Tang, J. Shang, and L. Kou, Janus WSSe Monolayer: An Excellent Photocatalyst for Overall Water Splitting, ACS Applied Materials & Interfaces 12, 29335 (2020).
- [27] P. Jamdagni, A. Kumar, S. Srivastava, R. Pandey, and K. Tankeshwar, Photocatalytic properties of anisotropic β -PtX2 (X = S, Se) and Janus β -PtSSe monolayers, Phys. Chem. Chem. Phys. **24**, 22289 (2022).
- [28] B. Zhou, A. Cui, L. Gao, K. Jiang, L. Shang, J. Zhang, Y. Li, S.-J. Gong, Z. Hu, and J. Chu, Enhancement effects of interlayer orbital hybridization in Janus MoSSe and tellurene heterostructures for photovoltaic applications, Phys. Rev. Mater. 5, 125404 (2021).
- [29] H. Zhao, Y. Gu, N. Lu, Y. Liu, Y. Ding, B. Ye, X. Huo, B. Bian, C. Wei, X. Zhang, and G. Yang, Janus In2SeTe for photovoltaic device applications from first-principles study, Chemical Physics 553, 111384 (2022).
- [30] M. J. Varjovi, M. Yagmurcukardes, F. M. Peeters, and E. Durgun, Janus two-dimensional transition metal dichalcogenide oxides: First-principles investigation of WXO monolayers with X=S, Se, and Te, Phys. Rev. B 103, 195438 (2021).
- [31] Z. Haman, M. Kibbou, N. Khossossi, E. Ouabida, P. Dey, I. Essaoudi, and A. Ainane, Harnessing intrinsic electric fields in 2D Janus MoOX (X=S, Se, and Te) monolayers for enhanced photocatalytic hydrogen evolution, International Journal of Hydrogen Energy 68, 566 (2024).
- [32] M. Bikerouin and M. Balli, Janus transition-metal dichalcogenides heterostructures for highly efficient excitonic solar cells, Applied Surface Science 598, 153835 (2022).
- [33] R. Chaurasiya, S. Tyagi, A. J. Kale, G. K. Gupta, R. Kumar, and A. Dixit, Advances in Physics and Chemistry of Transition Metal Dichalcogenide Janus Monolayers: Properties, Applications, and Future Prospects, Ad-

- vanced Theory and Simulations 8, 2400854 (2025).
- [34] A.-Y. Lu, H. Zhu, J. Xiao, C.-P. Chuu, Y. Han, M.-H. Chiu, C.-C. Cheng, C.-W. Yang, K.-H. Wei, Y. Yang, Y. Wang, D. Sokaras, D. Nordlund, P. Yang, D. A. Muller, M.-Y. Chou, X. Zhang, and L.-J. Li, Janus monolayers of transition metal dichalcogenides, Nature. Nanotech. 12, 744 (2017).
- [35] J. Zhang, S. Jia, I. Kholmanov, L. Dong, D. Er, W. Chen, H. Guo, Z. Jin, V. B. Shenoy, L. Shi, and J. Lou, Janus Monolayer Transition-Metal Dichalcogenides, ACS Nano 11, 8192 (2017).
- [36] Y.-C. Lin, C. Liu, Y. Yu, E. Zarkadoula, M. Yoon, A. A. Puretzky, L. Liang, X. Kong, Y. Gu, A. Strasser, H. M. I. Meyer, M. Lorenz, M. F. Chisholm, I. N. Ivanov, C. M. Rouleau, G. Duscher, K. Xiao, and D. B. Geohegan, Low Energy Implantation into Transition-Metal Dichalcogenide Monolayers to Form Janus Structures, ACS Nano 14, 3896 (2020).
- [37] R. Sant, M. Gay, A. Marty, S. Lisi, R. Harrabi, C. Vergnaud, M. T. Dau, X. Weng, J. Coraux, N. Gauthier, O. Renault, G. Renaud, and M. Jamet, Synthesis of epitaxial monolayer Janus SPtSe, npj 2D Mater Appl 4, 41 (2020).
- [38] B. S. Zainal, P. J. Ker, H. Mohamed, H. C. Ong, I. Fattah, S. A. Rahman, L. D. Nghiem, and T. M. I. Mahlia, Recent advancement and assessment of green hydrogen production technologies, Renewable and Sustainable Energy Reviews 189, 113941 (2024).
- [39] J. K. Nørskov, J. Rossmeisl, A. Logadottir, L. Lindqvist, J. R. Kitchin, T. Bligaard, and H. Jónsson, Origin of the Overpotential for Oxygen Reduction at a Fuel-Cell Cathode, The Journal of Physical Chemistry B 108, 17886 (2004).
- [40] A. Rahman, J. R. Jennings, A. L. Tan, and M. M. Khan, Molybdenum Disulfide-Based Nanomaterials for Visible-Light-Induced Photocatalysis, ACS Omega 7, 22089 (2022).
- [41] E. W. Keong Koh, C. H. Chiu, Y. K. Lim, Y.-W. Zhang, and H. Pan, Hydrogen adsorption on and diffusion through MoS2 monolayer: First-principles study, International Journal of Hydrogen Energy 37, 14323 (2012), hYFUSEN.
- [42] G. Tejaswini, A. E. Sudheer, M. Vallinayagam, M. Posselt, M. Zschornak, S. Maniprakash, and D. Murali, Band alignment in CdS-α-Te van der Waals heterostructures for photocatalytic applications: influence of biaxial strain and electric field, Phys. Chem. Chem. Phys. 26, 29339 (2024).
- [43] C. Karthikeyan, G. Tejaswini, A. E. Sudheer, M. Vallinayagam, M. Posselt, M. Zschornak, and D. Murali, Theoretical insights into PtSSe–SnSSe heterostructures for renewable energy applications, J. Mater. Chem. C 13, 11904 (2025).
- [44] J. Ma, J. Pang, J. Yang, W. Xie, X. Kuang, and A. Mao, Prediction of high photoconversion efficiency and photocatalytic water splitting in vertically stacked TMD heterojunctions MX2/WS2 and MX2/MoSe2 (M = Cr, Mo, W; X = S, Se, Te), J. Mater. Chem. A 13, 9312 (2025).
- [45] H. Xu, Y. Shen, X. Guo, and L. Zhang, A review of strategies to improve the performance of photocatalysts for CO2 reduction, Materials Today Chemistry 34, 101802 (2023).
- [46] Z. Chen, Y. Chi, H. Ma, S. Yuan, C. Hao, H. Ren, W. Zhao, H. Zhu, and W. Guo, Strain-Tunable Photo-

- catalytic Performance in Two-Dimensional Janus In2S2X (X=Se,Te) Monolayer as Photocatalyst for CO2 Reduction, ChemPhotoChem 7, e202300037 (2023).
- [47] X. Yu, Z. Peng, L. Xu, W. Shi, Z. Li, X. Meng, X. He, Z. Wang, S. Duan, L. Tong, X. Huang, X. Miao, W. Hu, and L. Ye, Manipulating 2D Materials through Strain Engineering, Small 20, 2402561 (2024).
- [48] T. Ouahrani, R. M. Boufatah, M. Benaissa, A. Morales-García, M. Badawi, and D. Errandonea, Effect of intrinsic point defects on the catalytic and electronic properties of Cu₂WS₄ single layer: Ab initio calculations, Phys. Rev. Mater. 7, 025403 (2023).
- [49] H. Mehdipour and P. Kratzer, Structural defects in a Janus MoSSe monolayer: A density functional theory study, Phys. Rev. B 106, 235414 (2022).
- [50] D. Maarisetty and S. S. Baral, Defect engineering in photocatalysis: formation, chemistry, optoelectronics, and interface studies, J. Mater. Chem. A 8, 18560 (2020).
- [51] Y. S. Hou, S. Ardo, and R. Q. Wu, Hybrid density functional study of band gap engineering of SrTiO₃ photocatalyst via doping for water splitting, Phys. Rev. Mater. 5, 065801 (2021).
- [52] M. M. Obeid, C. Stampfl, A. Bafekry, Z. Guan, H. R. Jappor, C. V. Nguyen, M. Naseri, D. M. Hoat, N. N. Hieu, A. E. Krauklis, T. V. Vu, and D. Gogova, First-principles investigation of nonmetal doped single-layer BiOBr as a potential photocatalyst with a low recombination rate, Phys. Chem. Chem. Phys. 22, 15354 (2020).
- [53] W. Thajitr, W. Busayaporn, D. P. Rai, and W. Sukkabot, Modulation of electronic and magnetic properties of MoX2 (X=S and Se) monolayer via mono- and cotransition metal dopants: Spin density functional theory, Physica Scripta 97, 095805 (2022).
- [54] Z. Zhang, K. Chen, Q. Zhao, M. Huang, and X. Ouyang, Effects of noble metal doping on hydrogen sensing performances of monolayer mos2, Materials Research Express 7, 015501 (2019).
- [55] H.-P. Komsa and A. Pasquarello, Finite-Size Supercell Correction for Charged Defects at Surfaces and Interfaces, Phys. Rev. Lett. 110, 095505 (2013).
- [56] J. DSchmidt, M. R. G. Marques, S. Botti, and M. A. L. Marques, Recent advances and applications of machine learning in solid-state materials science, npj Comput. Mater. 5, 83 (2019).
- [57] X. Cao, W. Luo, and H. Liu, A prediction model for CO2/CO adsorption performance on binary alloys based on machine learning", RSC Adv. 14, 12235 (2024).
- [58] Z. Yu, Y. Li, Y. Wen, B. Shan, and J. Yang, Machine learning prediction of hydrogen adsorption energy on platinum nanoclusters: A comparative study of SOAP descriptors, Computational and Theoretical Chemistry 1241, 114923 (2024).
- [59] V. Fung, G. Hu, P. Ganesh, and B. G. Sumpter, Machine learned features from density of states for accurate adsorption energy prediction, Nat Commun 12, 88 (2021).
- [60] N. P. Makhanya, M. Kumi, C. Mbohwa, and B. Oboirien, Application of machine learning in adsorption energy storage using metal organic frameworks: A review, Journal of Energy Storage 111, 115363 (2025).
- [61] B. H. Lee, J. Fatheema, D. Akinwande, and W. Wang, Understanding and predicting trends in adsorption energetics on monolayer transition metal dichalcogenides, npj 2D Mater Appl 9, 61 (2025).
- [62] W. Liu, N. Xu, Z. Li, M. Ma, X. Hu, Z.-K. Han, Y. Jiang,

- W. Yuan, H. Yang, S. V. Levchenko, and Y. Wang, Advancing the understanding and prediction accuracy of molecular adsorption energy with artificial intelligence, Phys. Rev. B 111, 195413 (2025).
- [63] P. G. Ghanekar, S. Deshpande, and J. Greeley, Adsorbate chemical environment-based machine learning framework for heterogeneous catalysis, Nat Commun 13, 5788 (2022).
- [64] G. Wang, Y. Wang, Y. Wang, T. Chen, L. Li, Z. Zhang, Z. Ding, X. Guo, Z. Luo, and X. Liu, Machine learningassisted design of transition metal-doped 2D WSn₂N₄ electrocatalysts for enhanced hydrogen evolution reaction, International Journal of Hydrogen Energy 90, 599 (2024).
- [65] M. Vallinayagam, J. Karthikeyan, M. Posselt, D. Murali, and M. Zschornak, Metalloid-doping in SMoSe Janus layers: first-principles study on efficient catalysts for the hydrogen evolution reaction, J. Mater. Chem. A 12, 7742 (2024).
- [66] G. Kresse and J. Furthmüller, Efficiency of ab-initio total energy calculations for metals and semiconductors using a plane-wave basis set, Comput. Mater. Sci. 6, 15 (1996).
- [67] P. E. Blöchl, Projector augmented-wave method, Phys. Rev. B 50, 17953 (1994).
- [68] J. P. Perdew, K. Burke, and M. Ernzerhof, Generalized Gradient Approximation Made Simple, Phys. Rev. Lett. 77, 3865 (1996).
- [69] H. J. Monkhorst and J. D. Pack, Special points for Brillouin-zone integrations, Phys. Rev. B 13, 5188 (1976).
- [70] G. Tejaswini, A. E. Sudheer, A. Kumar, P. K. Perepu, M. Vallinayagam, C. Kamal, S. M. Prakash, M.Posselt, M. Zschornak, and D. Murali, Hydrogen adsorption energy trends in Mo/WXY (X, Y = S, Se, Te) regular and Janus TMD monolayers: a first-principles and machine learning study, J. Mater. Chem. A, (2025).
- [71] H. Zong, G. Zeng, H. Miao, Z. Mo, X. Zhu, and H. Xu, Symmetry breaking induced local electron rearrangement to enhance photocatalytic tetracycline hydrochloride oxidation and hydrogen evolution of carbon nitride, Applied Surface Science 649, 158964 (2024).
- [72] M. Greenacre, P. J. F. Groenen, T. Hastie, A. I. D'Enza, A. Markos, and E. Tuzhilina, Principal component analysis, Nat. Rev. Methods. Primers. 2, 100 (2022).
- [73] M. Boubchir, R. Boubchir, and H. Aourag, The Principal Component Analysis as a tool for predicting the mechanical properties of Perovskites and Inverse Perovskites, Chemical Physics Letters 798, 139615 (2022).
- [74] R. O. Duda, P. E. Hart, and D. G. Stork, *Pattern Classification (2nd Edition)* (Wiley-Interscience, USA, 2000).
- [75] I. Goodfellow, Y. Bengio, and A. Courville, *Deep Learning* (MIT Press, 2016) book in preparation for MIT Press.
- [76] D. P. Kingma and J. Ba, Adam: A method for stochastic optimization (2017), arXiv:1412.6980 [cs.LG].
- [77] D. C. Liu and J. Nocedal, On the limited memory BFGS method for large scale optimization, Mathematical Programming 45, 503 (1989).
- [78] L. Bottou and O. Bousquet, The Tradeoffs of Large-Scale Learning, in *Optimization for Machine Learning* (The

- MIT Press, 2011).
- [79] F. Pedregosa, G. Varoquaux, A. Gramfort, V. Michel, B. Thirion, O. Grisel, M. Blondel, P. Prettenhofer, R. Weiss, V. Dubourg, J. Vanderplas, A. Passos, D. Cournapeau, M. Brucher, M. Perrot, and E. Duchesnay, Scikit-learn: Machine learning in Python, Journal of Machine Learning Research 12, 2825 (2011).
- [80] N. V. Chawla, K. W. Bowyer, L. O. Hall, and W. P. Kegelmeyer, Smote: Synthetic minority over-sampling technique, Journal of Artificial Intelligence Research 16, 321–357 (2002).
- [81] P. E. Blöchl, O. Jepsen, and O. K. Andersen, Improved tetrahedron method for Brillouin-zone integrations, Phys. Rev. B 49, 16223 (1994).
- [82] A. Huang, W. Shi, and Z. Wang, Optical Properties and Photocatalytic Applications of Two-Dimensional Janus Group-III Monochalcogenides, J. Phys. Chem. C 123, 11388 (2019).
- [83] P. Kumar, V. Sharma, S. N. Shirodkar, and P. Dev, Predicting phase preferences of two-dimensional transition metal dichalcogenides using machine learning, Phys. Rev. Mater. 6, 094007 (2022).
- [84] D. Willhelm, N. Wilson, R. Arroyave, X. Qian, T. Ca-gin, R. Pachter, and X. Qian, Predicting Van der Waals Heterostructures by a Combined Machine Learning and Density Functional Theory Approach, ACS Appl. Mater. Interfaces 14, 25907 (2022).
- [85] P. Han, J. Zhang, S. Shi, Y. Zhao, Y. Zhang, and J. Wang, Machine learning assisted screening of two dimensional chalcogenide ferromagnetic materials with Dzyaloshinskii Moriya interaction, npj Comput. Mater. 10, 232 (2024).
- [86] M. T. Dau, M. Al Khalfioui, A. Michon, A. Reserbat-Plantey, S. Vézian, and P. Boucaud, Descriptor engineering in machine learning regression of electronic structure properties for 2D materials, Sci. Rep. 13, 5426 (2023).
- [87] K. Sujata, N. Verma, R. G. Solanki, and A. Kumar, Ther-moelectric performance of Bi-based novel Janus mono-layer structures, Mater. Adv. 6, 849 (2025).
- [88] WebElements: (1993), last accessed 15th July 2025.
- [89] A. Kandemir and H. Sahin, Janus single layers of In₂SSe: A first-principles study, Phys. Rev. B 97, 155410 (2018).
- [90] P. Chauhan, J. Singh, and A. Kumar, Two-dimensional Janus antimony chalcohalides for efficient energy conversion applications, J. Mater. Chem. A 12, 16129 (2024).
- [91] M. Johnson-Groh, Breakthrough in green hydrogen energy production found in Janus materials, Scilight 2025, 191101 (2025).
- [92] A. O. M. Maka and M. Mehmood, Green hydrogen energy production: current status and potential, Clean Energy 8, 1 (2024).
- [93] M. K. Choudhary, A. R. V, G. S. S, and P. Ravindran, Composition and Structure Based GGA Bandgap Prediction Using Machine Learning Approach, Advanced Theory and Simulations n/a, e00771 (2025).
- [94] L. Ju, M. Bie, X. Tang, J. Shang, and L. Kou, Janus WSSe Monolayer: An Excellent Photocatalyst for Overall Water Splitting, ACS Applied Materials & Interfaces 12, 29335 (2020).